Lithos 196–197 (2014) 83–98

Contents lists available at ScienceDirect

Lithos

journal homepage: www.elsevier.com/locate/lithos

# Distinct sources for syntectonic Variscan granitoids: Insights from the Aguiar da Beira region, Central Portugal

M.M. Costa [a,*], A.M.R. Neiva [b], M.R. Azevedo [a], F. Corfu [c]

[a] GeoBioTec, Department of Geosciences, University of Aveiro, Campus de Santiago, 3810-193 Aveiro, Portugal
[b] Geosciences Centre, Department of Earth Sciences, University of Coimbra, Largo do Marquês de Pombal, 3000-272 Coimbra, Portugal
[c] Department of Geosciences, University of Oslo, PB1047 Blindern, N-0316 Oslo, Norway

ARTICLE INFO

*Article history:*
Received 26 June 2013
Accepted 27 February 2014
Available online 6 March 2014

*Keywords:*
Iberian Massif
Aguiar da Beira
Syntectonic granitoids
Geochemistry
Sr–Nd–O isotopes

ABSTRACT

The Variscan syntectonic granitoid plutons from the Aguiar da Beira region (central Portugal) were emplaced into metasediments of Late Proterozoic–Early Cambrian age during the last Variscan ductile tectonic event ($D_3$), which is related to dextral and sinistral shearing.

The older intrusion, with a U–Pb ID–TIMS zircon age of 321.8 ± 2.0 Ma, consists of porphyritic biotite granodiorite–granite with transitional I–S type geochemical signature, relatively low $^{87}Sr/^{86}Sr_{322}$ ratios (0.7070–0.7074), $\varepsilon Nd_{322}$ values of −3.9 to −4.6 and whole-rock and zircon $\delta^{18}O$ values of 10.6‰ and 8.0‰, respectively. By contrast, the younger intrusion is an S-type muscovite–biotite leucogranite, emplaced at 317.0 ± 1.1 Ma, showing more radiogenic $^{87}Sr/^{86}Sr_{317} = 0.7104$–$0.7146$, lower $\varepsilon Nd_{317}$ values of −7.7 to −8.7 and higher $\delta^{18}O$-wr = 11.3‰ and $\delta^{18}O$-zr = 9.5‰. The combined isotopic and geochemical evidence supports a lower crustal origin for the biotite granodiorite–granite, involving the anatexis of lower crustal metaigneous protoliths, and possible hybridization with mantle-derived magmas. A shallower origin, at mid crustal levels, from pure crustal derivation, through moderate degrees of partial melting of Proterozoic–Cambrian metasediments is proposed instead for the muscovite–biotite leucogranite.



## 1. Introduction

The Iberian Variscan belt, also known as Iberian Massif, was formed in Carboniferous times after the complete subduction of the Palaeozoic Rheic Ocean, during amalgamation of Pangea by the complex and polycyclic collision of Laurussia with Gondwana. Continental collision began around 365 Ma (Dallmeyer et al., 1997), with crustal thickening ($D_1$) and associated prograde metamorphism of Barrovian type. Continued shortening is thought to have been followed by the exhumation of the thickened continental crust ($D_2$) (e.g. Arenas and Catalán, 2003; Escuder Viruete et al., 1994; Martínez Catalán et al., 2009; Valle Aguado et al., 2005), and final deformation ($D_3$) is considered to be related to crustal-scale strike-slip ductile shear zones that produced large-wavelength upright folds (Martínez Catalán et al., 2009). Migmatization and low-pressure/high-temperature (LP–HP) metamorphism started during $D_2$, continued throughout $D_3$ and culminated with the emplacement of abundant syntectonic granitoids. Immediately after $D_3$, large volumes of late- to post-tectonic granite magmas intruded the Variscan continental crust, strongly overprinting its previous tectono-metamorphic record.

To other authors the tectono-metamorphic evolution of the Iberian Variscan belt is better explained as the result of two compressive deformation phases ($D_1$ and $D_2$), during which the crust reached its maximum thickness, followed by a late, post-thickening, ductile tectonic event ($D_3$) marking the end of the continental collision in Iberia (Dias and Ribeiro, 1995; Noronha et al., 1981; Ribeiro et al., 1990). However, the P–T conditions attained during $D_2$, inferred from the mineral assemblages related to the $S_2$ fabrics, are considered as a strong evidence for the extensional character of this event (Valle Aguado et al., 2005) in opposition to the compressive regime interpretation. Nevertheless, irrespective of the model accepted, $D_3$ is considered in both interpretations to be a post-thickening strike-slip phase responsible for the final structural arrangement of the Iberian Massif.

Regional constraints show that Variscan granite plutonism in Iberia post-dates syn-collisional deformation ($D_1 + D_2$), being predominantly correlated with intracontinental shearing ($D_3$). The diversity of granite types observed in this segment of the Variscan belt represents the sum of a series of processes, ranging from partial melting of distinct source rock materials, mixing and/or mingling of crustal- and mantle-derived magmas, fractional crystallization, crustal contamination and more complex models involving concurrent assimilation and fractional

* Corresponding author at: Starplan, Centre for Star and Planet Formation, Natural History Museum of Denmark, University of Copenhagen, Øster Voldgade 5-7, 1350 Copenhagen K, Denmark.
*E-mail addresses:* mmcosta@ua.pt (M.M. Costa), neiva@dct.uc.pt (A.M.R. Neiva), mazevedo@ua.pt (M.R. Azevedo), fernando.corfu@geo.uio.no (F. Corfu).

http://dx.doi.org/10.1016/j.lithos.2014.02.023
0024-4937/

crystallization (AFC) (e.g. Azevedo et al., 2005; Beetsma, 1995; Castro et al., 1999; Dias et al., 2002; Fernández-Suárez et al., 2011; Neiva and Gomes, 2001; Villaseca et al., 1999). In order to assess the factors controlling the evolution of each specific granitoid suite, it is crucial to understand the information stored in rock structures and to investigate the main vectors of chemical and isotopic change involved in their petrogenesis.

In this study petrographic, geochemical, Sr–Nd–O isotopic data and high-precision U–Pb ID–TIMS zircon and monazite ages are used to discuss the origin of two particular syntectonic intrusive suites from the central sector of the Central-Iberian Zone. The aim was to contribute to a better understanding of the origin, genesis and evolution of these magmas during the Variscan orogeny and constrain the nature of their potential sources, as well as the timing and duration of magmatic and deformation events in the studied area.

## 2. Geological background

Based on tectonostratigraphic criteria, the Iberian Variscan belt is divided into, from north to south, the Cantabrian, West Asturian-Leonese, Galicia-Trás-os-Montes, Central-Iberian, Ossa-Morena and South Portuguese zones (Fig. 1). In its internal domains, such as in the Central-Iberian Zone, where the study area is located, the stratigraphic record includes a Proterozoic Gondwanan basement of Cadomian (West African) affinity overlain by Early Palaeozoic, mostly siliciclastic sequences, deposited on the passive margin of northern Gondwana (e.g. Fernández-Suárez et al., 2002, 2011; Gutiérrez-Alonso et al., 2011; Martínez Catalán et al., 2007, 2009; Murphy et al., 2008; Robardet, 2002, 2003).

The Aguiar da Beira region is located within the axial zone of the Iberian Massif (Fig. 1), in central northern Portugal. The region is mainly composed of Variscan granitoids emplaced into Neoproterozoic–Early Palaeozoic sedimentary sequences, which were variably affected by regional metamorphism and deformation during the Variscan orogeny (Fig. 2). The oldest rocks exposed in this area belong to the so called "Schist–Greywacke Complex" (SGC), a thick turbidite-like formation of Neoproterozoic–Early Cambrian age consisting of metapelites and metagreywackes interlayered with relatively thin calc-silicate and metaconglomerate horizons (Oliveira et al., 1992; Rodríguez Alonso et al., 2004; Sousa, 1984). The SGC is unconformably overlain by an Ordovician clastic succession of stable marine platform sediments, spatially confined to the core of the NW–SE trending Porto–Sátão syncline that crosses the southwestern corner of the studied area (Fig. 1). A narrow deposit of Late Carboniferous molasse occurs in contact with the Ordovician rocks (Fig. 1).

The overall structure of the region can be ascribed to the combined effects of two main Variscan deformation events ($D_1 + D_3$). The first, $D_1$, affects all the pre-Carboniferous sequences and resulted in the generation of NW–SE striking subvertical folds with a penetrative axial plane schistosity ($S_1$), whilst $D_3$ is related to several crustal-scale transcurrent shear zones that have accommodated part of the shortening related to the final stages of the continental collision (Valle Aguado et al., 2005). One of these major shear zones, the NW–SE striking sinistral Douro–Beira shear zone, coincident with the Porto–Sátão syncline (Fig. 1), led to the development of a subvertical mylonitic $S_3$ fabric recorded in both the pre-Carboniferous and the Carboniferous metasedimentary units (Valle Aguado et al., 2005).

Regional metamorphism in this area corresponds to a low-grade metamorphic epizonal domain in which metamorphic recrystallization

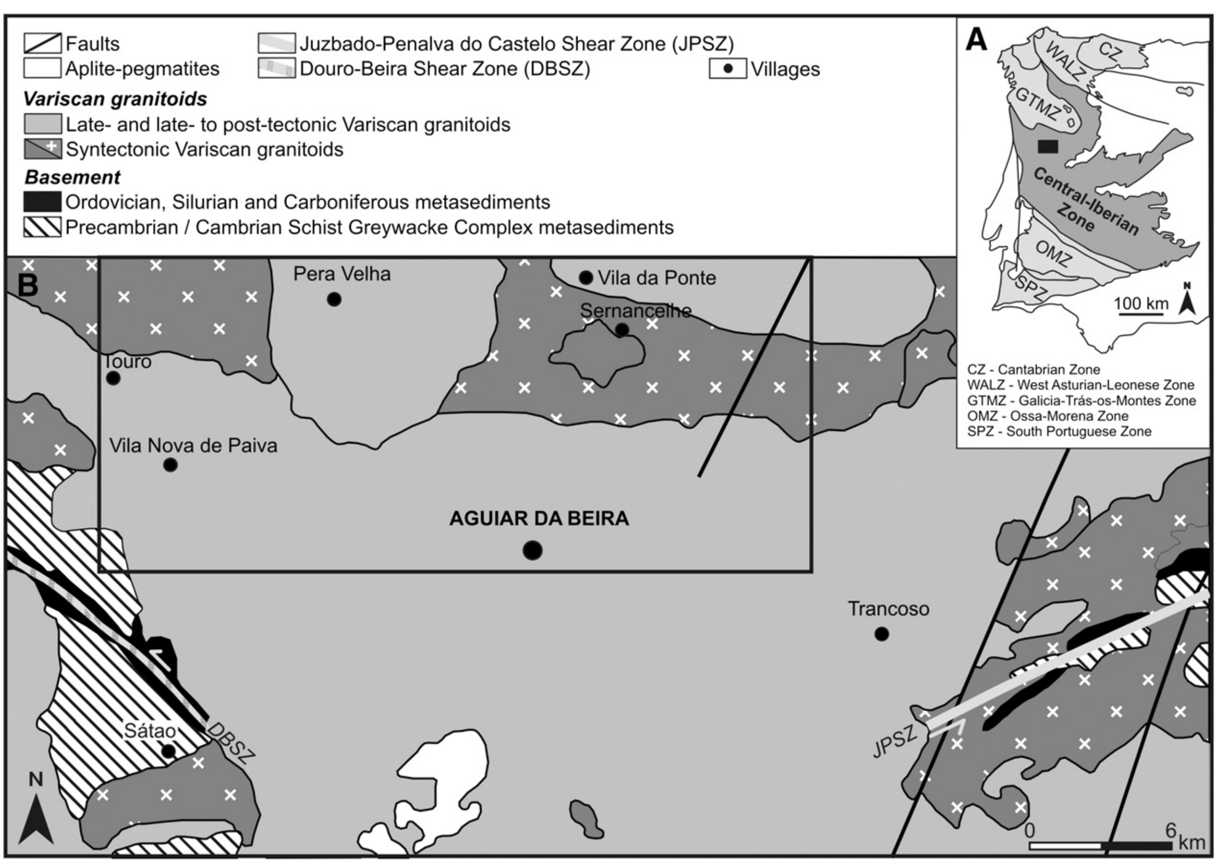


**Fig. 1.** A) Divisions of the Iberian Massif with location of the Aguiar da Beira region within the Central-Iberian Zone (redrawn from Sánchez-García et al., 2008); B) Geological map of part of the Beiras Batholith (adapted from Carta Geológica de Portugal à escala 1:1,000,000, LNEG, 2010) with identification of the Aguiar da Beira region.

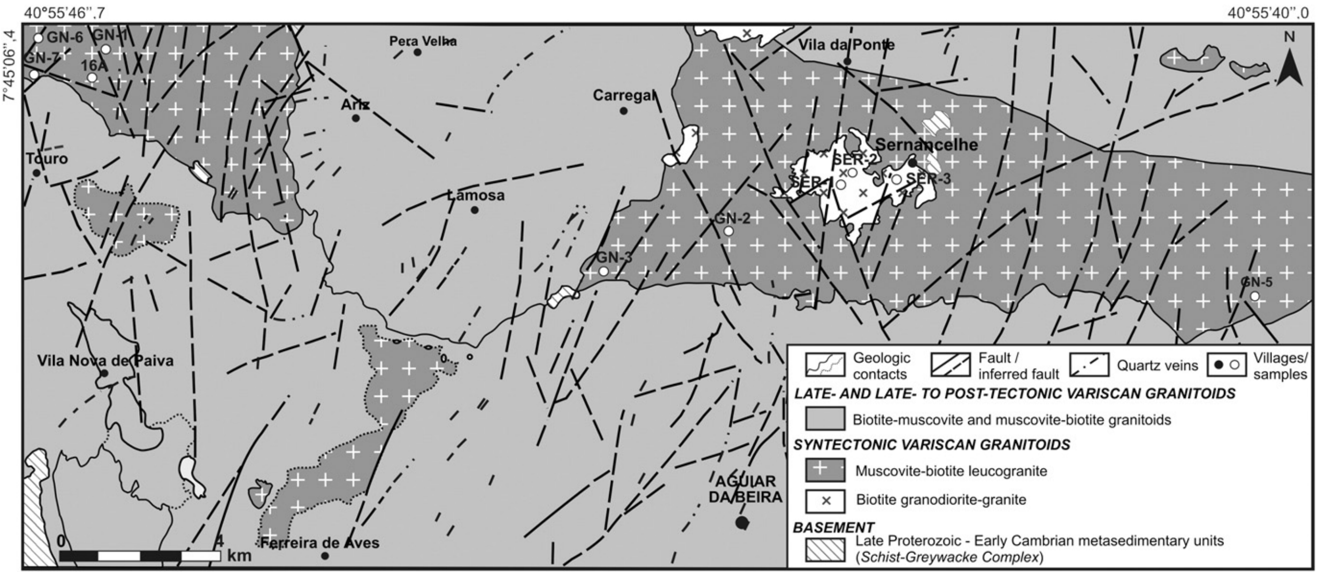


**Fig. 2.** Detailed geological map of the northern sector of the Aguiar da Beira region.
Modified from Teixeira et al. (1972).

occurred under greenschist facies conditions not exceeding the biotite zone. The emplacement of voluminous amounts of granitic magmas during and slightly after $D_3$ generated low-P–high-T contact aureoles.

Variscan intrusions, spanning the entire spectrum of granitoid types found in the NW Iberian Variscan belt, dominate the Aguiar da Beira region, covering about 75% of the total exposure (Fig. 2). The intrusive sequence consists of an earlier syntectonic (syn-$D_3$) association, which is described in detail below, and a volumetrically dominant late- to post-tectonic association formed by biotite monzogranites, biotite–muscovite granites and minor bodies of muscovite leucogranites.

## 3. Syntectonic association — field occurrence

The syn-$D_3$ association is composed of two intrusive suites with specific compositional, petrographic and geochemical characteristics: (a) an early biotite granodiorite–granite and (b) a slightly younger, highly peraluminous leucogranite. Zircon and/or monazite geochronology yield

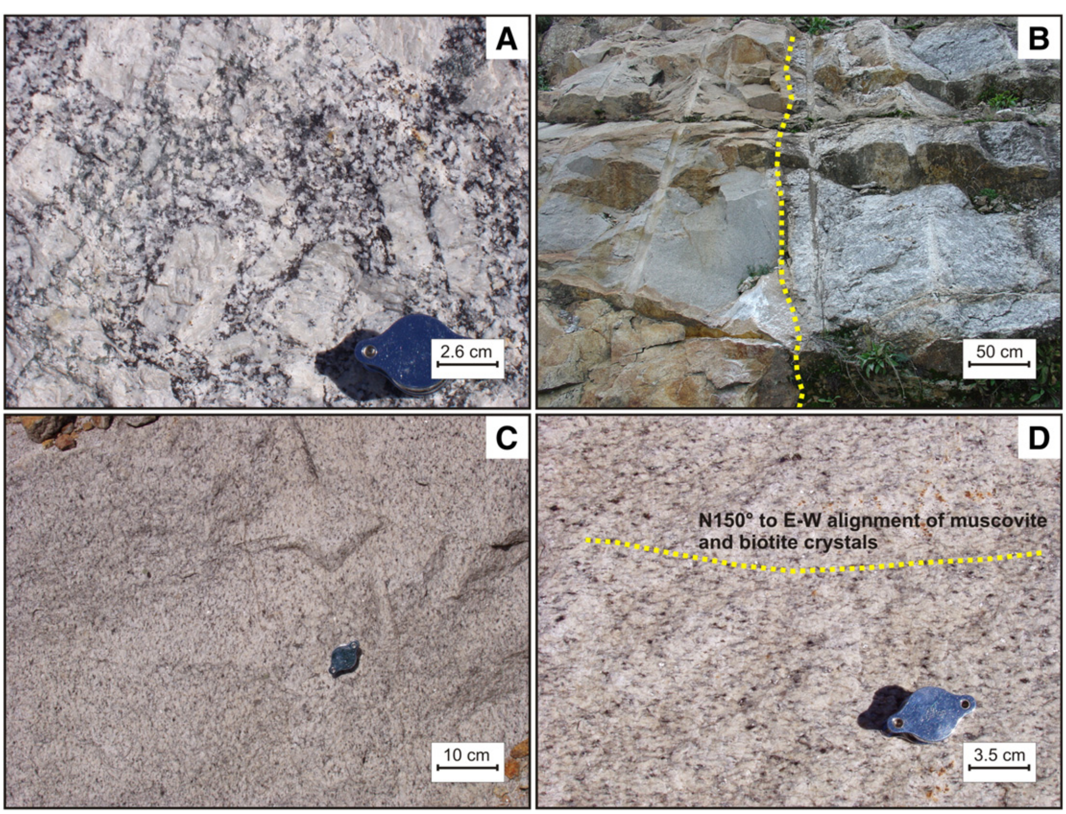


**Fig. 3.** Outcrop views of the two syntectonic intrusions from Aguiar da Beira region. A — close-up view of the biotite granodiorite–granite; B — contact between muscovite–biotite leucogranite (on the left) and biotite granodiorite–granite (on the right); C and D — overview (C) and close-up view (D) of the muscovite–biotite leucogranite.

U–Pb ages of 321.8 ± 2.0 Ma for the biotite granodiorite–granite and 317.0 ± 1.1 Ma for the highly peraluminous muscovite–biotite leucogranite (this study).

### 3.1. Syn-$D_3$ biotite granodiorite–granite

The medium- to coarse-grained porphyritic biotite granodiorite–granite forms an irregularly shaped intrusion of about 2 × 4 km and two smaller exposures in the northern part of the area (Fig. 2). All these occurrences are surrounded by the syn-$D_3$ muscovite–biotite leucogranite and seem to represent remnants of an earlier intrusive complex. The biotite granodiorite–granite (Fig. 3A) locally shows a N130° trending magmatic flow foliation, due to the alignment of K-feldspar megacrysts. The NW–SE foliation is concordant with $D_3$ regional structures and might be an evidence for syntectonic emplacement. Rounded and ellipsoidal mafic microgranular enclaves with sizes ranging from a few centimeters to several decimeters are common. As a result of an extensive interaction with the host granitoids, the original mineralogical, textural and geochemical characteristics of the mafic microgranular enclaves are no longer preserved. Some light colored enclaves of fine-grained granite with cognate appearance have also been observed.

### 3.2. Syn-$D_3$ highly peraluminous muscovite–biotite leucogranite

Unlike the biotite granodiorite–granite, the peraluminous leucogranite crops out as a large NW–SE to E–W trending intrusion with long and short axes of about 21 and 8 km, respectively (Fig. 2). Field relationships indicate emplacement during $D_3$, after the biotite granodiorite–granite previously described. The contacts between the two granitoids are sharp (Fig. 3B). A younger, circular, late- to post-tectonic granitoid pluton separates the leucogranite intrusion into two portions (Fig. 2). In the western part, the massif consists of a heterogeneously deformed medium-grained muscovite–biotite granite, showing a gneissic foliation (Fig. 3C, D) defined by the sub-parallel alignment of biotite and muscovite. This foliation is steeply inclined and runs parallel to the Douro–Beira $D_3$ transcurrent shear zone suggesting that the emplacement of this granite was controlled by shearing. In the eastern part, the granite is finer-grained and shows no evidence of solid state deformation. The absence of evidence for deformation in the whole eastern part of the muscovite–biotite leucogranite and in the biotite granodiorite–granite suggests that the Douro–Beira shear zone did not affect this sector. Mafic microgranular igneous enclaves are absent throughout the entire massif. By contrast, centimeter-sized xenoliths of metamorphic country-rocks are abundant.

## 4. Analytical procedures

Representative rock samples from the two intrusions were collected, crushed and milled to fine powders in an agate mortar for whole-rock geochemistry and Rb–Sr, Sm–Nd and $\delta^{18}O$ isotope analyses. Major- and trace-element data (including REE) were obtained by ICP-AES and ICP-MS, respectively, at the Activation Laboratories, Ltd. (Canada). Precision is better than 4% for major elements and 10% for trace elements. The detection limits are 0.001 wt.% for MnO and $TiO_2$, 0.01 wt.% for the remaining oxides, and lower than 1 ppm for most trace elements, except V and Pb (5 ppm), Cr and Ni (20 ppm), Cu (10 ppm) and Zn (30 ppm). FeO was determined by titration with a standardized potassium permanganate solution, at the Earth Sciences Department of the University of Coimbra, Portugal (precision ± 1%).

Whole-rock powders for strontium and neodymium isotope analyses were dissolved in a HF–$HNO_3$ mixture in pressurized Parr vessels for 3 days, then dried and taken up in HCl for chemical separation. Cation exchange resin (Biorad AG50W) in quartz glass columns was used to separate Sr and the REE fraction. Neodymium was separated from the other REE in quartz glass columns filled with LN-resin from Eichrom. $^{87}Sr/^{86}Sr$ and $^{143}Nd/^{144}Nd$ isotope ratios were measured on a VG Sector 54 mass spectrometer operating in dynamic mode, at the Laboratory of Isotope Geology of the University of Aveiro, Portugal. By maintaining a 1.5–2 V $^{88}Sr$ beam for 50–100 cycles, an internal precision of 20 ppm (1-sigma) on $^{87}Sr/^{86}Sr$ was consistently achieved. Fractionation was corrected with an exponential law relative to $^{86}Sr/^{88}Sr = 0.1194$. During the measuring campaign, the $^{87}Sr/^{86}Sr$ ratio of SRM-987 was 0.710249(6) (6 ppm, 1-sigma, n = 61; literature value = 0.710248). Neodymium isotope ratios were measured as metal ions in a Ta–Re–Ta triple filament assembly in a three sequence dynamic routine using seven Faraday cups. By maintaining a 1 V $^{144}Nd$ beam for 50–100 cycles, an internal precision of 20 ppm (1-sigma) was obtained. The $^{143}Nd/^{144}Nd$ ratios were corrected for mass fractionation using the $^{146}Nd/^{144}Nd$ ratio of 0.7219. Repeated analysis of the JNdi-1 standard gave an average value of 0.5121037(41) for 16 measurements. Analytical blanks for Sr and Nd are lower than 250 pg. The Rb, Sr, Sm and Nd concentrations used for calculation of $^{87}Rb/^{86}Sr$ and $^{147}Sm/^{144}Nd$ isotope ratios were obtained either by isotopic dilution or by ICP-MS at the Activation Laboratories, Canada. The initial εNd values were calculated using $^{147}Sm/^{144}Nd = 0.1967$ and $^{143}Nd/^{144}Nd = 0.512638$ for the Chondritic Uniform Reservoir (CHUR) following Jacobsen and Wasserburg (1980). A linear model with parameters $^{147}Sm/^{144}Nd = 0.2136$ and $^{143}Nd/^{144}Nd = 0.513151$ was used for the Depleted Mantle reservoir (DM) according to Goldstein and Jacobsen (1988).

Oxygen-isotope analyses of whole-rock samples were performed by gas mass spectrometry according to the methodology of Clayton and Mayeda (1963), at the Department of Earth Sciences of the University of Western Ontario, Canada. Repeated analysis of biotite NBS-30 and quartz NBS-28 standards gave values of 4.99‰ and 9.72‰, respectively.

Mineral compositions were determined with a Cameca Camebax SX-100 electron microprobe at the Scientific-Technological Centre of the University of Oviedo, Spain, operating in wavelength dispersive mode with an acceleration voltage of 15 kV and a beam current of 15 nA. Analytical precision was better than 2%.

Zircons and monazites, used for isotope dilution TIMS U–Pb analyses, were separated from <420 μm size fractions by standard mineral separation techniques using a Frantz® magnetic separator and heavy liquids. The crystals were subsequently handpicked under a binocular microscope and mechanically abraded to remove external disturbed domains (Davies et al., 1982; Krogh, 1982). On the basis of optical microscopy the best quality zircon grains (free of visible cracks, overgrowths or inclusions) were cleaned with $HNO_3$, acetone and ultra-pure $H_2O$. A

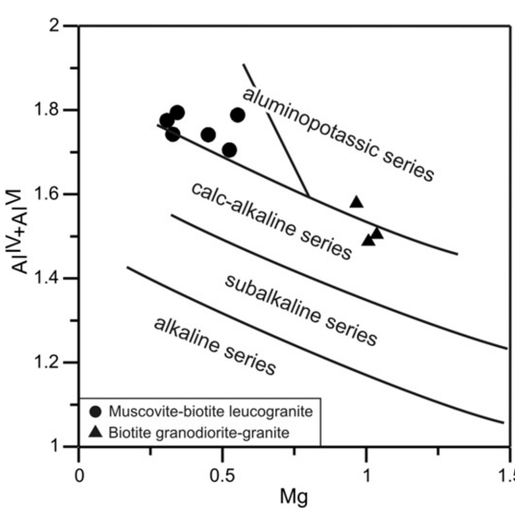


**Fig. 4.** Aluminium and magnesium compositions of biotite (atoms per 11 O) from the Aguiar da Beira syntectonic granitoids. Fields from different magmatic series taken from Nachit et al. (1985).

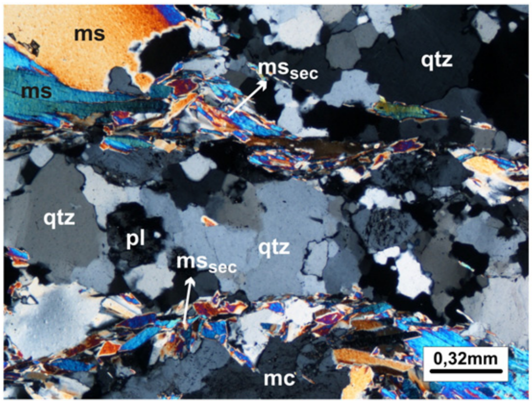


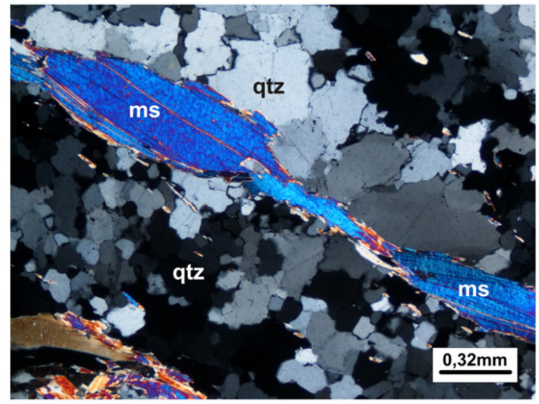


**Fig. 5.** Microphotographs (crossed polars) of the muscovite–biotite leucogranite representing some aspects of the subsolidus deformation observed on the western sector of the intrusion. The left picture shows the gneissic foliation, characterized by the alignment of micas (biotite not shown in this picture) alternated with quartz and feldspar bands. On the right photograph the alignment of muscovite flakes is also visible, as well as some details of ductile deformation, like the lenticular shape of these crystals or the bending of cleavages on the rightmost crystal (intracrystalline strain), together with evidences of brittle deformation, as the subgranulation of quartz and its irregular boundaries. These aspects evidence the tectonic strain that affected the muscovite–biotite leucogranite during its emplacement.

mixed $^{202}Pb–^{205}Pb–^{235}U$ tracer solution was added prior to dissolution. Chemical separation and purification of uranium and lead were performed in small Teflon® columns, according to the procedure described by Krogh (1973) and modified by Corfu (2004). Uranium and lead isotopic compositions were measured on a Finnigan MAT 262 multicollector mass spectrometer at the Department of Geosciences of the University of Oslo, Norway. The samples, as well as a mixed NBS 982Pb + U500 standard, were loaded on single rhenium filaments using a silica-gel activator and $H_3PO_4$. Total procedure blanks were ≤2 pg for lead and 0.1 pg for uranium. Initial Pb was corrected using Stacey and Kramers (1975) model compositions. Decay constants are from Jaffey et al. (1971). U–Pb age parameters were calculated using ISOPLOT 3 Microsoft Excel *add-in* (Ludwig, 2003).

Oxygen isotopic analyses on individual zircon crystals from the same samples (SER-3 and GN-3), morphologically similar to the ones selected for U–Pb geochronology, were obtained at the NORDSIM facility (Swedish Museum of Natural History, Stockholm, Sweden). The crystals were mounted in epoxy resin disks, ground, polished and then coated with 30 nm of gold. The isotopic ratios were measured during two different sessions using a CAMECA IMS-1270 multicollector-equipped ion microprobe. The basic instrument setup and analytical procedure closely follow the methodology described by Whitehouse and Nemchin (2009). Analytical acquisition was performed measuring reference zircon 91500, with an assumed $\delta^{18}O$ value of 9.86‰ (Wiedenbeck et al., 2004), four times at the beginning and end of a session, and twice between each block of four sample analyses. Small linear drift corrections (<0.01‰ per run) were applied to each of the data sessions in order to minimize the external error, which was 0.24‰ and 0.26‰ (1SD) for the first and second session respectively. Twelve spot analyses were obtained from seven crystals of the biotite granodiorite–granite sample (SER-3) and eight from seven crystals of the muscovite–biotite leucogranite (GN-3). The analyzed crystals were inspected by cathodoluminescence and backscattered electron imaging techniques. No evidence of inheritance was identified in the grains utilized for the oxygen work. The individual analyses and averages are listed in Appendix 1.

The trace element composition of minerals was determined at the National Oceanographic Centre of the University of Southampton, United Kingdom, on 250 μm polished sections, with a New Wave UP193FX laser ablation system coupled to a Thermo X-Series II ICP-MS. Small polished chips of NIST 610 and NIST 612 standards were used for calibration (See the Electronic Appendix, Table 2E). Prior to each analysis a gas (Ar/He) blank was measured and subtracted from the following analyses. Before and after each sample set, the NIST 612 and 610 standards were analyzed using the same laser parameters used for the samples (see Electronic Appendix, Table 2E). Five repeats of each standard and blank measurement were averaged and used to produce a 2-point calibration curve. The standard data were internally normalized to the $^{44}Ca$ signal. The data acquisition was performed at a pulse rate of 7 Hz, for 20 s. The laser shot diameter was 35 μm. The comparison of the counts-per-second, measured for each element in the standard relative to its known concentration, allows the determination of the calibration factors that were applied to all sample data.

## 5. Petrography and mineral chemistry

### 5.1. Syn-$D_3$ biotite granodiorite–granite

The syn-$D_3$ medium- to coarse-grained porphyritic biotite granodiorite–granite contains quartz (22–25%), plagioclase (27–44%), microcline (12–36%), biotite (12–20%), apatite, zircon, monazite and ilmenite. Quartz is characteristically interstitial and shows undulatory extinction. Plagioclase ($An_{20}$–$An_{33}$) occurs in the matrix of the rock as weakly zoned subhedral crystals containing small inclusions of biotite, quartz and apatite. Strontium contents in plagioclase are high (608–1168 ppm; see Electronic Appendix, Table 2A) and define irregular zoning patterns, suggesting disequilibrium crystallization conditions. K-feldspar is slightly perthitic microcline and constitutes large phenocrysts, up to 7 × 3 cm, with compositions ranging from $Or_{85}$ to $Or_{96}$, enclosing quartz, plagioclase and biotite. Microcline is also present in the groundmass as small interstitial crystals ($Or_{80}$–$Or_{96}$). Myrmekitic intergrowths are common at the contacts between K-feldspar and plagioclase. Biotite is the dominant mafic mineral. It is subhedral, strongly pleochroic ($\alpha$: light yellow; $\gamma = \beta$: foxy-red brown) and carries abundant inclusions of accessory minerals. Biotite compositions are characterized by high $TiO_2$ (2.92–3.30 wt.%), Ba (407–589 ppm) and V (214–234 ppm) contents, low $Al_2O_3$ (16.71–18.03 wt.%) and $Fe^{2+}$ / ($Fe^{2+}$ + Mg) (~0.54) values and plot in the field of calc-alkaline, low oxidation Mg-biotite (Fig. 4; Table 2C — Electronic Appendix). Accessory minerals include long prismatic to acicular apatite crystals, subhedral to anhedral zircon and monazite grains with marked radiation halos in biotite and primary opaque oxides (ilmenite). Secondary muscovite and chlorite were identified as alteration phases.

### 5.2. Syn-$D_3$ highly peraluminous muscovite–biotite leucogranite

The syn-$D_3$ leucogranite is a medium- to fine-grained muscovite-biotite equigranular granite composed of quartz (32–37%), perthitic microcline (26–36%), plagioclase (16–23%), muscovite (4–11%), biotite (0–6%), and minor amounts of tourmaline, zircon, apatite, monazite and ilmenite (very scarce). In the more deformed samples, a gneissic foliation defined by the alignment of muscovite and biotite flakes can be observed. Quartz is mostly anhedral and shows undulose extinction. K-feldspar is perthitic microcline ($Or_{87}$–$Or_{97}$) and occurs as anhedral interstitial crystals, frequently enclosing small inclusions of plagioclase, biotite and muscovite. In the samples affected by regional deformation, the primary K-feldspar crystals are often recrystallized into a mosaic of smaller grains of K-feldspar, albitic plagioclase and quartz (Fig. 5). Plagioclase ($An_0$–$An_7$) is essentially subhedral, weakly zoned and may show bent twin lamellae and recrystallization borders in the more deformed samples. The Sr and Ba contents in plagioclase are uniformly low (Sr = 4–36 ppm; Ba = 0–2 ppm), suggesting near equilibrium crystallization conditions. Biotite has a foxy red-brown color and is often intergrown with muscovite. In intensively deformed domains, the micas are concentrated into long bands and the larger crystals may exhibit sigmoidal shapes (Fig. 5). Biotite compositions ($Al_{total}$ = 1.65–1.79 apfu; $Fe^{2+}/(Fe^{2+}+Mg)$ = 0.72–0.83) are typical of biotites from aluminopotassic associations (Fig. 4). Primary muscovite constitutes well-developed subhedral crystals with a rather restricted range of XFe (0.55–0.76), reflecting the high degree of geochemical fractionation of this granite. Small subhedral tourmaline grains, pleochroic in yellow and yellow-blue hues, were identified only in the more deformed samples. Secondary muscovite occurs as sheaf-like aggregates replacing feldspar, or as newly formed microflakes surrounding primary muscovite, or filling cracks in the matrix.

## 6. ID–TIMS U–Pb geochronology

One sample from the syn-$D_3$ biotite granodiorite-granite (SER-3) and one sample from the syn-$D_3$ muscovite–biotite leucogranite (GN-3) were selected for U–Pb geochronology. The U–Pb isotope data for zircon and monazite are compiled in Table 1.

### 6.1. Biotite granodiorite–granite (sample SER-3)

The zircons from this sample are generally euhedral, translucent, short to medium prismatic and light yellow in color. Some of these zircons may show bi-pyramidal terminations. Inclusions are relatively rare. Xenocrystic zircons may be present as separate grains or as cores in more equant grains. To minimize the danger of inheritance, long prismatic crystals have been preferentially selected for isotope analysis. Long prismatic morphologies are associated with rapid crystallization (Corfu et al., 2003).

A total of six zircon fractions were analyzed. The results are listed in Table 1 and plotted in a Concordia diagram in Fig. 6A. All the analyzed zircon fractions are slightly discordant, probably as the result of some Pb loss, and show no evidence of having old Pb inheritance. A regression line using all six fractions yields an upper intercept age of 321.9 ± 2.0 Ma, which is considered to represent the age of igneous crystallization of the biotite granodiorite–granite.

Three monazite fractions consisting of equant anhedral to subhedral yellowish grains plot reversely discordant (Fig. 6A). One monazite fraction provides a $^{207}Pb/^{235}U$ age of 326 ± 8.6 Ma that agrees within error with the zircon upper intercept age. The other two monazite ages (314 and 316 Ma) are clearly younger, suggesting that they may have been partially reset during the intrusion of the nearby syn-tectonic muscovite–biotite leucogranite (Fig. 2). As shown by several authors, monazite is not strongly affected by diffusive lead loss (Cherniak and Watson, 2000; Cherniak et al., 2004; Poitrasson et al., 1996), but may be partly reset by younger magmatic events (Bosse et al., 2009; Poitrasson et al., 1996, 2000; Seydoux-Guillaume et al., 2002). Fluid interaction can promote monazite recrystallization (Hawkins and Bowring, 1997; Teufel and Heinrich, 1997; Townsend et al., 2001), even at low temperatures (Karioris et al., 1981). The close spatial association between the biotite

**Table 1**
TIMS U–Pb data obtained in zircon and monazite fractions of the two syntectonic granitoids from the Aguiar da Beira region.

| Analyzed fractions | Weight (µg) | U[a] (ppm) | Th/U[b] | Pbc[c] (pg) | $^{206}Pb/^{204}Pb$[d] | $^{207}Pb/^{235}U$[e] | 2σ (abs) | $^{206}Pb/^{238}U$[e] | 2σ (abs) | Rho | $^{207}Pb/^{206}Pb$[e] | 2σ (abs) | Age (Ma) $^{206}Pb/^{238}U$[e] | 2σ (abs) | $^{207}Pb/^{235}U$[e] | 2σ (abs) | $^{207}Pb/^{206}Pb$[e] | 2σ (abs) | D[f] (%) |
|---|---|---|---|---|---|---|---|---|---|---|---|---|---|---|---|---|---|---|---|
| *Biotite granodiorite–granite – sample SER-3* | | | | | | | | | | | | | | | | | | | |
| Zr – 3 lp | 1 | 1157 | 0.25 | 6.1 | 605 | 0.35777 | 0.00225 | 0.04931 | 0.00015 | 0.5 | 0.05262 | 0.00029 | 310.3 | 0.9 | 310.5 | 1.7 | 312.3 | 12.3 | 0.7 |
| Zr – 10 tips | 13 | 1414 | 0.16 | 14 | 4117 | 0.36427 | 0.00092 | 0.04998 | 0.0001 | 0.9 | 0.05286 | 0.00006 | 314.4 | 0.6 | 315.4 | 0.7 | 322.7 | 2.5 | 2.6 |
| Zr – 1 lp | 1 | 2286 | 0.19 | 6.8 | 1074 | 0.3663 | 0.00169 | 0.0502 | 0.00016 | 0.7 | 0.05292 | 0.00017 | 315.8 | 1 | 316.9 | 1.3 | 325.2 | 7.5 | 3 |
| Zr – 3 lp | 1 | 715 | 0.14 | 1.1 | 1939 | 0.35351 | 0.00193 | 0.0485 | 0.00017 | 0.65 | 0.05286 | 0.00022 | 305.3 | 1 | 307.4 | 1.4 | 322.8 | 9.4 | 5.6 |
| Zr – 1 lp | 1 | 301 | 0.13 | 1.5 | 641 | 0.35965 | 0.00431 | 0.0492 | 0.00017 | 0.47 | 0.05301 | 0.00057 | 309.6 | 1.1 | 312 | 3.2 | 329.3 | 24.2 | 6.1 |
| Zr – 1 lp | 3 | 2112 | 0.12 | 7.3 | 2736 | 0.36157 | 0.00131 | 0.04969 | 0.00015 | 0.87 | 0.05277 | 0.0001 | 312.6 | 0.9 | 313.4 | 1 | 319.1 | 4.1 | 2.1 |
| Mz – 2 cryst. | 1 | 2472 | 20.19 | 4.4 | 1797 | 0.36548 | 0.00189 | 0.05069 | 0.00025 | 0.71 | 0.0523 | 0.0002 | 318.7 | 1.5 | 316.3 | 1.4 | 298.4 | 8.8 | −7 |
| Mz – 1 cryst. | <1 | >277 | 18.49 | 4.5 | 211 | 0.36245 | 0.00711 | 0.05001 | 0.00019 | 0.39 | 0.05256 | 0.00097 | 314.6 | 1.2 | 314 | 5.3 | 309.9 | 41.5 | −1.6 |
| Mz – 1 cryst. | 1 | 140 | 23.05 | 2.8 | 181 | 0.37791 | 0.01182 | 0.05186 | 0.00018 | 0.55 | 0.05285 | 0.00156 | 326 | 1.1 | 325.5 | 8.7 | 322.3 | 65.7 | −1.2 |
| *Muscovite–biotite leucogranite – sample GN-3* | | | | | | | | | | | | | | | | | | | |
| Zr – 1 tip | 1 | 582 | 0.37 | 2.1 | 876 | 0.36625 | 0.00314 | 0.05044 | 0.00017 | 0.51 | 0.05266 | 0.00039 | 317.2 | 1.1 | 316.9 | 2.3 | 314.2 | 16.8 | −1 |
| Zr – 3 fr | 1 | 784 | 0.65 | 2.9 | 868 | 0.36386 | 0.00281 | 0.05016 | 0.00021 | 0.63 | 0.05261 | 0.00032 | 315.5 | 1.3 | 315.1 | 2.1 | 312.2 | 13.6 | −1.1 |
| Zr – 3 fr | 1 | 342 | 0.76 | 1.3 | 848 | 0.3667 | 0.00361 | 0.05005 | 0.00022 | 0.55 | 0.05314 | 0.00044 | 314.8 | 1.4 | 317.2 | 2.7 | 334.7 | 18.6 | 6.1 |
| Zr – 1 lp | 1 | 2448 | 0.09 | 8.9 | 873 | 0.36168 | 0.00169 | 0.04985 | 0.00013 | 0.61 | 0.05262 | 0.00020 | 313.6 | 0.8 | 313.5 | 1.3 | 312.4 | 8.4 | −0.4 |
| Zr – 1 tip | 1 | 727 | 0.11 | 156.2 | 34 | 0.46854 | 0.09919 | 0.05276 | 0.0014 | 0.3 | 0.06441 | 0.01322 | 331.4 | 8.6 | 390.2 | 66.4 | 755 | 100 | 57.5 |
| Mz – 1 crystal | 1 | 22,289 | 9.37 | 5.3 | 12,536 | 0.34485 | 0.00088 | 0.04782 | 0.00011 | 0.93 | 0.0523 | 0.00005 | 301.1 | 0.7 | 300.8 | 0.7 | 298.6 | 2.1 | −0.9 |

Zr – zircon; Mz – monazite; lp – long prismatic crystal; fr – fragments of a large prismatic crystal; cryst – crystal; [a,c]weight and concentrations are known to be better than 10%, except for those near and below the limit of resolution of the balance (1 µg). [b]Th/U model ratio inferred from 208/206 ratio and age of the sample. [c]Pbc is total common Pb in the sample (initial + blank). [d]Raw data corrected for fractionation; [e]corrected for fractionation, spike, blank and initial common Pb; error calculated by propagating the main sources of uncertainty; initial common Pb corrected using Stacey and Kramers (1975) model Pb. [f]Degree of discordance.

granodiorite–granite and the muscovite–biotite leucogranite suggests that the emplacement of the latter may have triggered monazite recrystallization.

*6.2. Muscovite–biotite leucogranite (sample GN-3)*

Sample GN-3 from the muscovite–biotite leucogranite yielded a much lower amount of zircon crystals than the sample from the biotite granodiorite–granite. Zircons extracted from this sample are transparent, pale yellow to colorless and practically devoid of inclusions. Small, rounded euhedral crystals and short prisms are dominant, but some long prismatic crystals were also identified. Given the scarcity of long prismatic zircons, the fractions selected for analysis include tips and long prismatic grains (two fractions) and fragments of a large abraded crystal (~350 × 630 μm) (two fractions). The four zircon fractions yielded a spread of concordant ages between 314 Ma and 317 Ma (Fig. 6B), reflecting partial Pb loss. The oldest concordant zircon age (317.2 ± 1.1 Ma) gives the best approximation to the crystallization age of the intrusion. Regression passing through the four zircon fractions results in an upper intercept age of 315.0 ± 6.1 Ma (Fig. 6B) providing further support for the age obtained.

The only monazite fraction analyzed from this granite consists of small rounded and ovoid grains and yielded an almost concordant $^{207}Pb/^{235}U$ age of 300.8 ± 0.7 Ma, which is significantly younger than the age of coexisting zircon. As mentioned before, the U–Pb monazite ages can be partially reset during late thermal events. In the Aguiar da Beira region, the effects of a younger overprint associated with the emplacement of large volumes of late-to post-tectonic granitoids, with ages of ≈300 Ma, may have been the principal cause for lowering the monazite age of the muscovite–biotite leucogranite.

## 7. Whole-rock geochemistry

Representative whole-rock chemical analyses for the two syntectonic granitoid intrusions from the Aguiar da Beira region are given in Table 2. The biotite granodiorite–granite is slightly peraluminous (A/CNK = 1.01–1.02) with very homogeneous $SiO_2$ contents (65.59–67.61 wt.%). Its composition plots essentially within the field of the monzogranites in the $R_1$–$R_2$ diagram (Fig. 7), defines an "alumino-cafemic" association of calk-alkaline type in the A–B diagram (Fig. 8A), and plots in the magnesian granite field in the Fe number vs. % $SiO_2$ diagram (Fig. 8$B_1$). Amongst the trace elements, Sr abundances are as great as 735 to 772 ppm, Ba reaches values of 1397–1691 ppm, Zr = 202–223 ppm (Fig. 9), and ΣREE ranges from 474 to 507 ppm. Chondrite normalized REE patterns for the biotite granodiorite–granite samples are characterized by high LREE/HREE ratios ($La_N/Lu_N$ = 55–58) and small Eu negative anomalies (Eu/Eu* = 0.71–0.80) (Fig. 10). In the multi-element variation diagrams normalized to primordial mantle there are strong negative anomalies for Nb, Ta, Sr, P and Ti and a positive anomaly for Th (Fig. 11A). The significant Ba and Sr enrichment, A/CNK values <1.1, highly fractionated REE patterns, and marked LILE/HFSE enrichment are typical of high-K calc-alkaline I-type magmas (Roberts and Clemens, 1993; Wilson, 1989).

By contrast, the Aguiar da Beira muscovite–biotite leucogranite is strongly peraluminous (A/CNK = 1.18 and 1.36) with high contents of silica (71.91–73.90 wt.%) and $P_2O_5$ (0.39–0.48 wt.%) and high Rb/Sr ratios (5–17), coupled with low CaO (0.29–0.63 wt.%), MgO (0.14–0.41 wt.%), Ba (81–295 ppm), Sr (31–77 ppm) and ΣREE (41–158 ppm) abundances. These rocks are classified as syenogranites in the $R_1$–$R_2$ diagram (Fig. 7) and plot in the leucogranitoid field of the peraluminous domain in the A–B classification diagram (Fig. 8A). The diagrams by Frost et al. (2001) also evidence the lower contents of MgO and CaO that characterize this leucogranite (Fig. 8$B_1$ and $B_2$). Despite their relatively narrow compositional range, the samples of this intrusion define coherent evolutionary curvilinear trends in most major- and trace-element variation diagrams, characterized by an increase in $SiO_2$, F, Rb, Cs and Ta and a decrease in $TiO_2$, MgO, CaO, $K_2O$, V, Zr, Sr, Ba, Hf and Th with decreasing total FeO (Fig. 9, Table 2), suggesting fractionation of feldspar, biotite and accessory minerals. Their REE chondrite normalized patterns are sub-parallel, moderately to strongly fractionated ($La_N/Lu_N$ = 15.8–68.8) and display increasing Eu negative anomalies with magmatic differentiation (Eu/Eu* = 0.48–0.28) (Fig. 10). Primordial mantle-normalized diagrams show marked negative anomalies in Nb, Sr and Ti and positive anomalies for Rb and K (Fig. 11B). Based on its major and trace element compositions, the two-mica leucogranite bears a strong resemblance to other S-type granitoids from the Iberian Variscan belt.

The temperature at which zircon starts to crystallize depends on the amount of zirconium present in the melt and this relation can be used as a geothermometer (Watson and Harrison, 1983). Zircon saturation temperatures ($T_{Zr}$) calculated from bulk rock compositions are 796 °C for the biotite granodiorite–granite and 731 °C for the muscovite–biotite leucogranite. Due to possible occurrence of zircons with inheritance in both intrusions, particularly in the muscovite–biotite leucogranite, the obtained $T_{Zr}$ are probably overestimated (Miller et al., 2003). However,

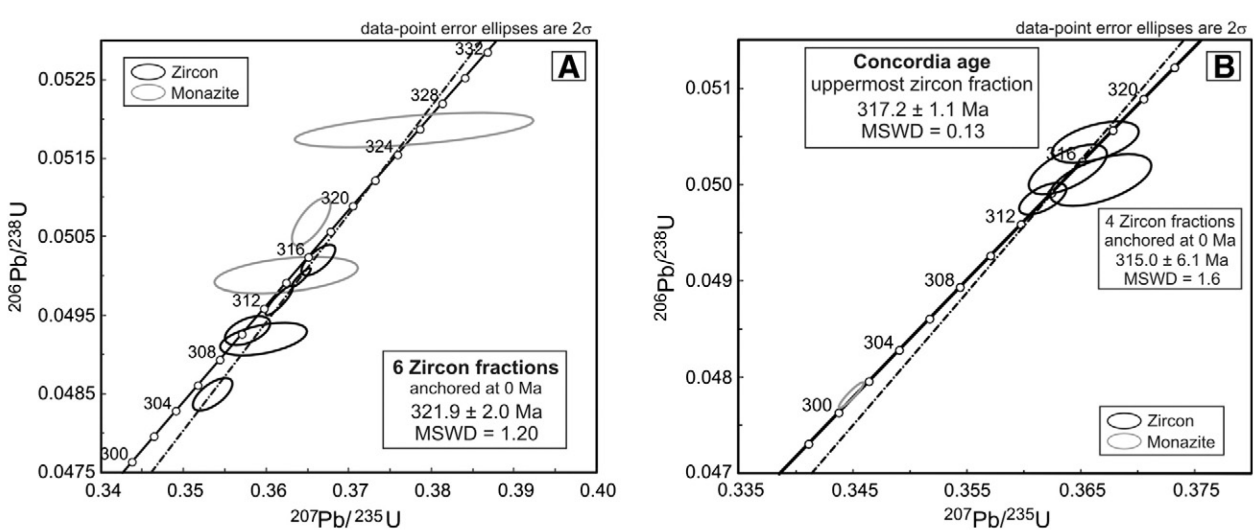


**Fig. 6.** U–Pb Concordia diagrams for zircon and monazite from the syntectonic granitoids of the Aguiar da Beira region. A — biotite granodiorite–granite; B — muscovite–biotite leucogranite.

the higher T estimates for the biotite granodiorite–granite are broadly consistent with the petrogenetic models discussed in a later section.

## 8. Sr–Nd and $\delta^{18}O$ (whole-rock and zircon) isotopic data

The Rb–Sr, Sm–Nd and oxygen isotopic data for the samples of the Aguiar da Beira syntectonic intrusions are listed in Table 3. As shown in the $^{87}Sr/^{86}Sr_i$–$\varepsilon Nd_i$ diagram (Fig. 12), the biotite granodiorite–granite has relatively low $^{87}Sr/^{86}Sr_{322}$ ratios (0.7070–0.7074) and $\varepsilon Nd_{322}$ varying between −3.9 and −4.6, while the muscovite–biotite leucogranite shows distinctly more radiogenic Sr isotopic signatures ($^{87}Sr/^{86}Sr_{317}$ = 0.7104–0.7146) and lower $\varepsilon Nd_{317}$ values (−7.7 to −8.7). One sample from the muscovite–biotite leucogranite (GN-6) has a much lower $^{87}Sr/^{86}Sr_{317}$ of 0.70495, probably reflecting a disturbance in the Rb–Sr isotopic system. Its high Rb/Sr ratio of 57 (vs. 12–31 in the others) suggests a recent introduction of Rb or Sr loss. The Nd model ages ($T_{DM}$) (DePaolo, 1981, 1988) range between 1.0 and 1.1 Ga in the biotite granodiorite–granite and between 1.6 and 2.1 Ga in the muscovite–biotite leucogranite.

Whole-rock oxygen isotopic compositions are high and match the trend observed in Nd and Sr, with higher values of $\delta^{18}O$-wr = 11.33‰ and $\delta^{18}O$-zr = 9.5 ± 0.2‰ in the leucogranites than in the granodiorite which is characterized by lower $\delta^{18}O$-wr = 10.6‰ and $\delta^{18}O$-zr = 8.0 ± 0.2‰.

## 9. Discussion

### 9.1. Time constraints

The U–Pb zircon crystallization ages of the Aguiar da Beira syntectonic granitoids provide time constraints for the duration of magmatic and tectonic events in the area and give new insights

**Table 2**
Major (wt.%) and trace (ppm) element composition of the Aguiar da Beira syntectonic granitoids.

| | Biotite granodiorite–granite | | | Muscovite–biotite leucogranite | | | | | | |
|---|---|---|---|---|---|---|---|---|---|---|
| | SER-2 | SER-3 | SER-1 | GN-5 | 16 A | GN-2 | GN-3 | GN-7 | GN-1 | GN-6 |
| $SiO_2$ | 65.59 | 66.51 | 67.61 | 71.91 | 72.22 | 72.44 | 72.57 | 73.00 | 73.01 | 73.90 |
| $TiO_2$ | 0.47 | 0.47 | 0.46 | 0.18 | 0.18 | 0.12 | 0.26 | 0.14 | 0.16 | 0.08 |
| $Al_2O_3$ | 16.59 | 15.90 | 15.60 | 15.09 | 15.27 | 14.91 | 15.14 | 14.86 | 14.67 | 15.27 |
| FeO | 2.49 | 2.53 | 2.44 | 1.21 | 0.96 | 0.96 | 1.06 | 0.69 | 0.90 | 0.44 |
| $Fe_2O_3$ | 0.43 | 0.44 | 0.41 | 0.05 | 0.10 | 0.01 | 0.22 | 0.16 | 0.11 | 0.09 |
| MnO | 0.05 | 0.05 | 0.05 | 0.02 | 0.02 | 0.03 | 0.02 | 0.02 | 0.02 | 0.02 |
| MgO | 1.25 | 1.29 | 1.20 | 0.41 | 0.26 | 0.19 | 0.31 | 0.19 | 0.24 | 0.14 |
| CaO | 2.45 | 2.39 | 2.30 | 0.62 | 0.47 | 0.53 | 0.63 | 0.37 | 0.56 | 0.29 |
| $Na_2O$ | 3.41 | 3.13 | 3.17 | 3.11 | 3.17 | 3.58 | 3.30 | 3.25 | 3.49 | 3.35 |
| $K_2O$ | 5.76 | 5.81 | 5.43 | 5.81 | 5.43 | 4.96 | 5.76 | 5.04 | 4.97 | 4.77 |
| $P_2O_5$ | 0.47 | 0.48 | 0.44 | 0.48 | 0.41 | 0.39 | 0.41 | 0.41 | 0.43 | 0.42 |
| F | 0.10 | 0.11 | 0.11 | 0.08 | 0.13 | 0.15 | 0.19 | 0.16 | 0.18 | 0.13 |
| S | 0.03 | 0.02 | 0.02 | 0.00 | 0.00 | 0.00 | 0.00 | 0.00 | 0.00 | 0.00 |
| LOI | 0.57 | 0.61 | 0.70 | 1.14 | 1.55 | 0.95 | 0.78 | 1.73 | 1.01 | 1.58 |
| Total | 99.80 | 99.88 | 100.10 | 100.10 | 100.10 | 99.17 | 100.60 | 99.93 | 99.68 | 100.40 |
| A/CNK | 1.02 | 1.01 | 1.02 | 1.20 | 1.28 | 1.22 | 1.18 | 1.30 | 1.21 | 1.36 |
| Li | 127 | 115 | 140 | 100 | 258 | 245 | 288 | 314 | 335 | 227 |
| Be | 6 | 5 | 5 | 5 | 5 | 5 | 4 | 5 | 8 | 10 |
| V | 54 | 58 | 51 | 7 | 10 | 6 | 8 | udl | 7 | 5 |
| Zn | 70 | 70 | 70 | 70 | 80 | 80 | 110 | 60 | 80 | 40 |
| Ga | 25 | 25 | 24 | 24 | 29 | 27 | 31 | 29 | 25 | 30 |
| Rb | 242 | 232 | 245.3 | 349 | 448 | 447 | 475 | 489 | 452 | 538 |
| Sr | 772 | 753 | 735 | 77 | 45 | 45 | 56 | 37 | 42 | 31 |
| Y | 21.5 | 21.1 | 20.4 | 13.6 | 6.9 | 6.2 | 7.3 | 5.3 | 5.6 | 5.1 |
| Zr | 202 | 223 | 203 | 82 | 75 | 52 | 106 | 59 | 65 | 46 |
| Nb | 13.6 | 13.7 | 14.7 | 13.4 | 12.3 | 12.9 | 8.6 | 12.8 | 11.7 | 16.9 |
| Sn | 8 | 8 | 6 | 16 | 15 | 14 | 7 | 20 | 19 | 31 |
| Cs | 12.1 | 13.5 | 11.5 | 19.7 | 37.6 | 19.5 | 14.8 | 42.3 | 46 | 50 |
| Ba | 1685 | 1691 | 1397 | 295 | 153 | 113 | 191 | 131 | 130 | 81 |
| Hf | 4.9 | 5.3 | 4.9 | 2.5 | 2.1 | 1.6 | 3 | 1.8 | 2 | 1.7 |
| Ta | 1.34 | 1.2 | 1.3 | 2.64 | 2.5 | 2.07 | 1.07 | 2.89 | 3.51 | 7.13 |
| W | 0.7 | udl | 0.6 | 2.1 | 2.1 | 1.8 | 0.8 | 2.5 | 2.8 | 4.3 |
| Tl | 1.46 | 1.38 | 1.44 | 1.99 | 2.89 | 3.1 | 2.89 | 2.88 | 2.94 | 3.49 |
| Pb | 68 | 67 | 71 | 32 | 27 | 26 | 28 | 21 | 23 | 19 |
| Bi | 0.1 | 0.2 | 0.1 | 1.5 | 3 | 2.9 | 1 | 3.1 | 1.8 | 2.8 |
| Th | 35.3 | 35.8 | 35 | 5.76 | 12.1 | 5.48 | 24.4 | 9.59 | 10.2 | 4.07 |
| U | 7.63 | 5.46 | 7.36 | 6 | 6.25 | 6.86 | 22.5 | 8.11 | 18.3 | 7.09 |
| La | 125 | 126 | 116 | 14.9 | 19.1 | 9.4 | 29.1 | 15.2 | 16 | 7.9 |
| Ce | 233 | 239 | 224 | 33 | 44.4 | 21.3 | 72.5 | 35.1 | 37 | 17.8 |
| Pr | 24.4 | 25.3 | 23.7 | 3.76 | 5.12 | 2.43 | 8.74 | 4.1 | 4.33 | 2.03 |
| Nd | 84.4 | 86.7 | 80.8 | 15 | 18.9 | 9.31 | 33.6 | 15.6 | 15.9 | 7.88 |
| Sm | 12 | 12.3 | 11.8 | 3.71 | 4.23 | 2.15 | 6.97 | 3.48 | 3.72 | 1.8 |
| Eu | 2.52 | 2.47 | 2.22 | 0.516 | 0.335 | 0.308 | 0.373 | 0.294 | 0.28 | 0.169 |
| Gd | 6.54 | 6.45 | 6.48 | 3.22 | 2.73 | 1.67 | 3.78 | 2.24 | 2.49 | 1.43 |
| Tb | 0.86 | 0.84 | 0.86 | 0.61 | 0.39 | 0.27 | 0.46 | 0.32 | 0.36 | 0.24 |
| Dy | 4.17 | 4 | 4.01 | 3 | 1.5 | 1.29 | 1.7 | 1.24 | 1.4 | 1.13 |
| Ho | 0.67 | 0.66 | 0.66 | 0.37 | 0.19 | 0.18 | 0.21 | 0.14 | 0.18 | 0.15 |
| Er | 1.8 | 1.74 | 1.71 | 0.82 | 0.44 | 0.45 | 0.49 | 0.33 | 0.41 | 0.36 |
| Tm | 0.25 | 0.235 | 0.234 | 0.104 | 0.059 | 0.067 | 0.066 | 0.047 | 0.052 | 0.052 |
| Yb | 1.51 | 1.52 | 1.43 | 0.6 | 0.35 | 0.41 | 0.37 | 0.28 | 0.3 | 0.34 |
| Lu | 0.217 | 0.228 | 0.197 | 0.076 | 0.045 | 0.053 | 0.046 | 0.033 | 0.04 | 0.05 |
| ΣREE | 497.3 | 507.4 | 474.1 | 79.7 | 97.8 | 49.3 | 158.4 | 78.4 | 82.5 | 41.3 |

udl — under the detection limit.

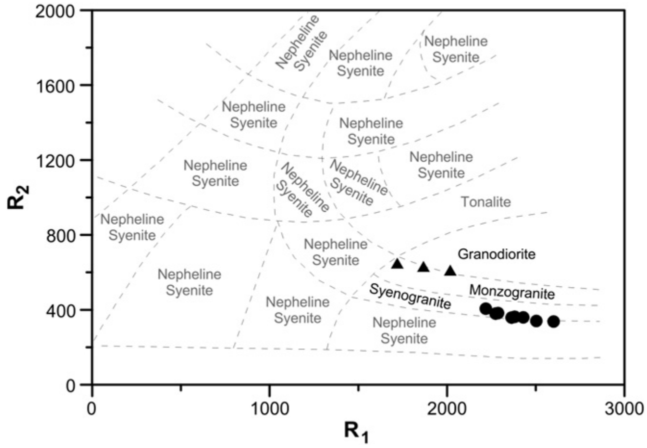


**Fig. 7.** Granitoid classification according to La Roche et al. (1980) $R_1$–$R_2$ diagram, $R_1 = 4Si - 11(Na + K) - 2(Fe + Ti)$ and $R_2 = 6Ca + 2 Mg + Al$. Symbols as in Fig. 4.

into the tectonothermal evolution of this sector of the Iberian Variscan belt. The Variscan plutonic activity started with the intrusion of the biotite granodiorite–granite, at c. 322 Ma, and was shortly followed by the emplacement of the muscovite–biotite leucogranite,

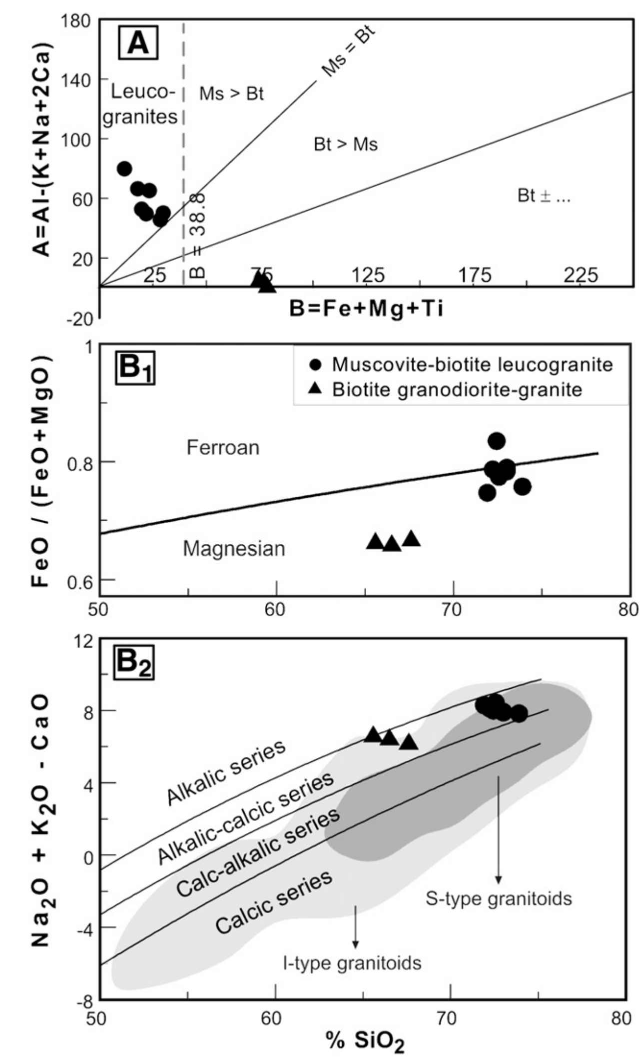


**Fig. 8.** A — composition of the Aguiar da Beira syntectonic granitoids in the diagram of Debon and Lefort (1988). Ms — muscovite; Bt — biotite. B — classification diagrams by Frost et al. (2001), $B_1$ — *Fe-number* diagram, FeO / (FeO + MgO) vs weight per cent $SiO_2$, and $B_2$ — modified alkali-lime index (MALI) diagram.

at c. 317 Ma. As both granitoids were intruded synkinematically during $D_3$, these ages reveal that the last Variscan ductile deformation event spanned a minimum of about 5 Ma. They also yield an upper age limit for the movement of the sinistral Douro–Beira shear zone which has controlled the emplacement of the muscovite–biotite leucogranite (c. 317 Ma). The geochronological data obtained in this study partially overlap the U–Pb ages determined for other syntectonic granitoids from the NW Iberian Variscan belt (Dias et al., 1998, 2002; Fernández-Suárez et al., 2000; Teixeira et al., 2012; Valle Aguado et al., 2005) and are consistent with the structural and metamorphic evolution proposed for this sector of the CIZ (e.g. Valle Aguado et al., 2005).

### 9.2. Magma sources

The compositional and isotopic differences between the syntectonic biotite granodiorite–granite and the muscovite–biotite leucogranite from Aguiar da Beira strongly suggest that these magmas were either produced by partial melting of distinct source rocks, or that different petrogenetic processes were involved in their origin (partial melting and/or magma mixing).

#### 9.2.1. Biotite granodiorite–granite

The major and trace element characteristics of the biotite granodiorite–granite are typical of metaluminous to slightly peraluminous high-K calc-alkaline I-type magmas with A/CNK values $<1.1$, significant Ba and Sr enrichment, high K/Rb ratios, fractionated REE patterns, marked LILE/HFSE enrichment, and negative anomalies of Nb–Ta, Ti, Y and HREE. This favors an origin by partial melting of feldspar-rich metaigneous crustal protoliths (high Ba and Sr), leaving a residue depleted in feldspar and biotite and enriched in mineral phases capable of retaining Nb, Ta, Ti, Y and HREE (rutile, iron oxides, garnet). Given the relatively fractionated character of this granite ($SiO_2 = 65.59$–$67.61$ wt.%), some additional contribution of fractional crystallization at deeper levels cannot be excluded. The Sr–Nd–$\delta^{18}O$ isotopic signature ($^{87}Sr/^{86}Sr_i = 0.7070$–$0.7074$, $\varepsilon Nd_i = -3.9$ to $-4.6$, $\delta^{18}O$-wr $= 10.57$–$10.59$‰) is consistent with the suggested mechanism. The initial Sr and Nd values overlap with those of the igneous lower crustal felsic granulite xenoliths from the Spanish Central System (Fig. 12) supporting an origin through partial melting of similar sources. Whole-rock $\delta^{18}O$ ($\delta^{18}O$-wr) and zircon $\delta^{18}O$ ($\delta^{18}O$-zr) values of 10.6‰ and 8.0‰, respectively, are common in felsic meta-igneous granulites (Hoefs, 2004).

The lower crustal felsic xenoliths plotted in Fig. 12 have been interpreted as the residues left after the extraction of granitic melts from lower crustal sources (Villaseca et al, 1999), and they suggest that the composition of the lower crust underneath Iberia, although not accurately known, might be more felsic and LILE and REE enriched than model compositions proposed for other areas (McLennan and Taylor, 1996; Villaseca et al., 1999; Wedepohl, 1995). The hypothetical derivation of the biotite granodiorite–granite from a protolith similar to that which produced the residual felsic xenoliths, is not only supported by their matching Sr and Nd isotopic signatures (Fig. 12), but also by the trace element composition (Fig. 11A). The compositions of a lower crustal xenolith and of an I-type granite from the Spanish Central System are plotted together with the biotite granodiorite–granite samples in a multielement diagram (Fig. 11A). The I-type granites have been considered and successfully modeled as representing melts extracted from the deep crust (Villaseca et al., 2009). The patterns for the three samples are similarly shaped which evidences their compositional resemblances and does not exclude a possible origin through the anatexis of similar protoliths as the ones that generated the SCS I-type granitoids. However their relationship is not straightforward and could be the result of several important factors, such as different degrees of partial melting, or/and the not well constrained behavior of accessory phases during melting, or even the effect of fractional crystallization processes.

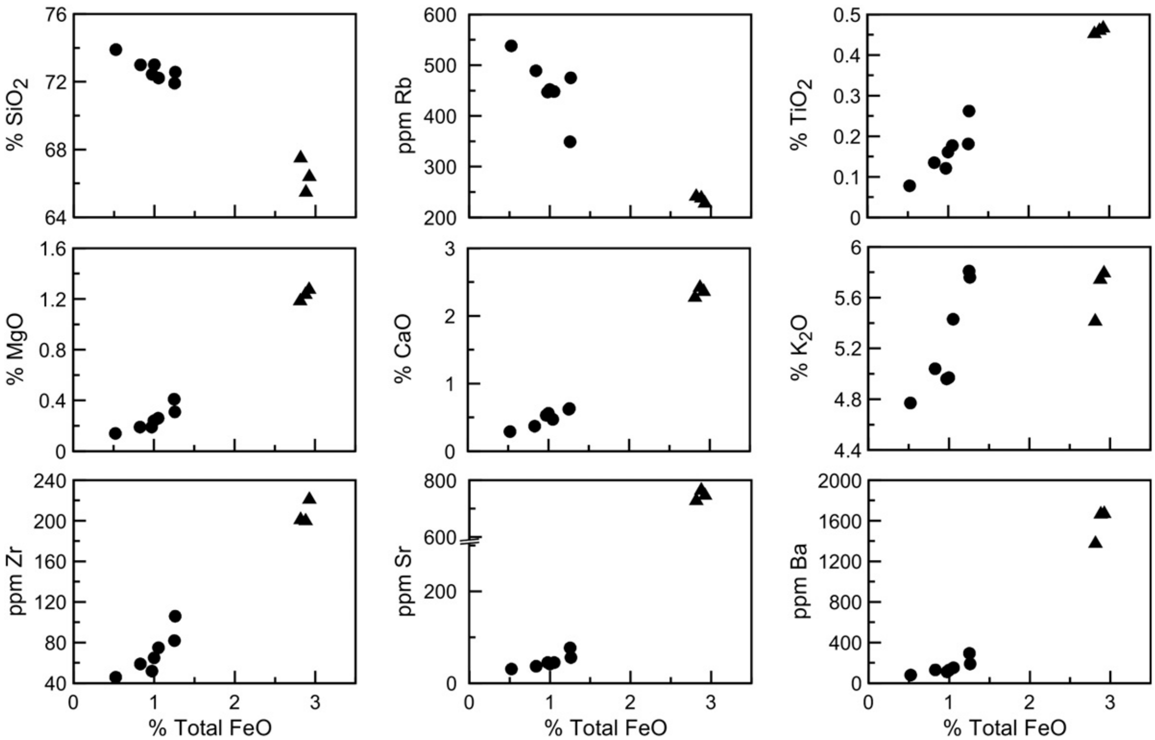


**Fig. 9.** Selected major (wt.%) and trace (ppm) element variation diagrams for the Aguiar da Beira syntectonic granitoids. Symbols as in Fig. 4.

Much of the chemical and isotope composition of this intrusion can alternatively be explained by simple mixing between metaluminous basic magmas of mantle origin and crust-derived peraluminous partial melts and/or AFC-type processes. The widespread occurrence of mafic microgranular enclaves would be consistent with hybridization processes between coeval mafic and felsic magmas (e.g. Barbarin, 2005; Barbarin and Didier, 1992; Vernon, 1984, 1990, 1991). In the Iberian Variscan belt, mafic igneous rocks and I-type or transitional S–I type granitoids with low degrees of crustal contamination yield $T_{DM}$ values ranging between ca. 0.95 and 1.2 Ga (Beetsma, 1995; Castro et al., 2003; Dias et al., 1998; Fernández-Suárez et al., 2011). These low $T_{DM}$ ages may imply some input of juvenile mantle magmas into the crust and, in this case, the $T_{DM}$ ages would correspond to mixed model ages between the juvenile source and an older crustal contaminant (Beetsma, 1995; Dias et al., 1998). However, these values can also result from a metaigneous basement extracted from a subcontinental enriched lithospheric mantle between ca. 0.9 and 1.1 Ga (Fernández-Suárez et al., 2011; Murphy et al., 2008).

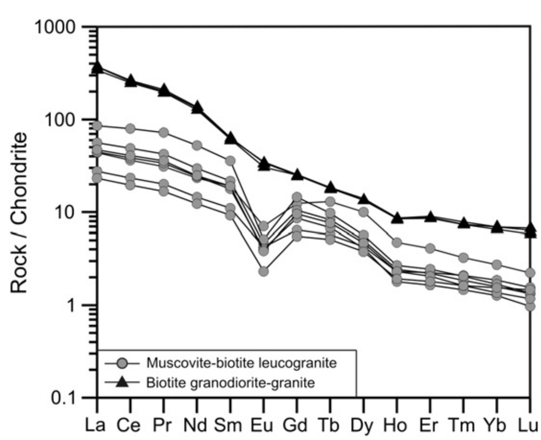


**Fig. 10.** Chondrite-normalized REE patterns for the samples of the two syntectonic granitoids from Aguiar da Beira. Normalizing values from Haskin et al. (1968).

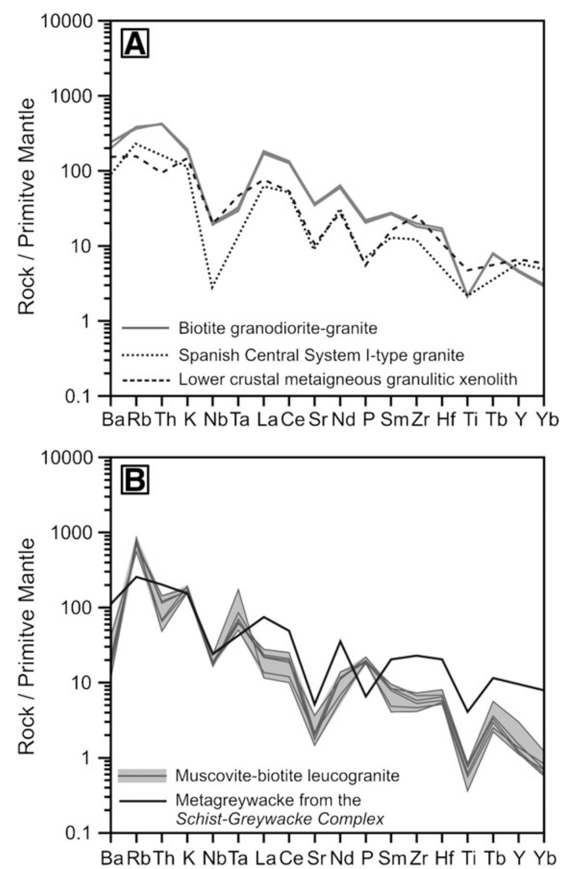


**Fig. 11.** Trace-element composition of the Aguiar da Beira syntectonic granitoids (normalizing values from Sun and McDonough, 1989). A — biotite granodiorite–granite samples, Spanish Central System I-type granite composition and lower crustal metaigneous granulitic xenolith sample (Villaseca et al., 1999); B — muscovite–biotite leucogranite samples and metagreywacke sample from the Schist–Greywacke Complex (Teixeira, 2008).

**Table 3**
Sr and Nd isotope data for the Aguiar da Beira region syntectonic granitoids.

| Sample | Rb[a] | Sr[a] | $^{87}Rb/^{86}Sr$ | ±2σ | $^{87}Sr/^{86}Sr$ | ±2σ | $(^{87}Sr/^{86}Sr)_t$ | εSr | Sm | Nd | $^{147}Sm/^{144}Nd$ | ±2σ | $^{143}N\backslash{}^{144}Nd$ | ±2σ | $(^{143}Nd/^{144}Nd)_t$ | $\varepsilon Nd_t$ | $T_{DM}$ (Ga) | $\delta^{18}O$-wr | $\delta^{18}O$-zr |
|---|---|---|---|---|---|---|---|---|---|---|---|---|---|---|---|---|---|---|---|
| *Biotite granodiorite–granite* | | | | | | | | | | | | | | | | | | | |
| SER-1 | 245 | 735 | 0.965 | 0.027 | 0.711810 | 0.000033 | 0.70739 | 46.33 | 11.8 | 80.8 | 0.088 | 0.002 | 0.512210 | 0.000013 | 0.51202 | −3.90 | 1.0 | 10.59 | – |
| SER-2 | 242 | 772 | 0.907 | 0.026 | 0.711330 | 0.000028 | 0.70717 | 43.26 | 12.0 | 74.4 | 0.098 | 0.003 | 0.512194 | 0.000012 | 0.51199 | −4.59 | 1.1 | 10.57 | – |
| SER-3 | 232 | 753 | 0.892 | 0.025 | 0.711100 | 0.000031 | 0.70701 | 41.01 | 12.3 | 86.7 | 0.086 | 0.002 | 0.512201 | 0.000016 | 0.51202 | −3.97 | 1.0 | – | 8.0 ± 0.3 |
| *Muscovite-biotite leucogranite* | | | | | | | | | | | | | | | | | | | |
| 16A | 455 | 45 | 29.64 | 0.840 | 0.845696 | 0.000057 | 0.71199 | 111.59 | | | – | – | – | – | – | – | – | – | – |
| GN-2 | 381 | 35 | 31.55 | 0.890 | 0.852726 | 0.000051 | 0.71037 | 88.59 | 2.2 | 9.31 | 0.140 | 0.004 | 0.512076 | 0.000009 | 0.51179 | −8.66 | 1.9 | – | – |
| GN-3 | 470 | 55 | 24.93 | 0.710 | 0.823760 | 0.000044 | 0.71128 | 101.46 | 6.97 | 33.6 | 0.125 | 0.004 | 0.512073 | 0.000013 | 0.51181 | −8.15 | 1.6 | – | 9.5 ± 0.2 |
| GN-5 | 329 | 75 | 12.81 | 0.360 | 0.772403 | 0.000042 | 0.71459 | 148.55 | 3.71 | 15.0 | 0.150 | 0.004 | 0.512133 | 0.000009 | 0.51182 | −7.96 | 2.1 | – | – |
| GN-6 | 548 | 28 | 57.59 | 1.600 | 0.964766 | 0.000075 | 0.70495 | 11.58 | 1.8 | 7.88 | 0.138 | 0.004 | 0.512121 | 0.000015 | 0.51183 | −7.73 | 1.8 | 11.33 | – |

Rb, Sr, Sm and Nd contents in ppm; Sr and Nd initial isotopic ratios calculated for the U–Pb age of each intrusion (322 Ma for the biotite granodiorite–granite, 317 Ma for the muscovite–biotite leucogranite); $\delta^{18}O$ data in ‰; $\delta^{18}O$-zr are average values – individual point analyses can be found in Appendix 1; – not determined.
[a] Rb and Sr composition of the muscovite–biotite leucogranite samples were determined by isotope dilution mass spectrometry (IDMS), whether the Rb and Sr contents of the biotite granodiorite–granite samples and all the Sm and Nd contents were determined by ICPMS.

Thus, the possible lineage of the biotite granodiorite–granite suite remains controversial, as the available data do not allow effective discrimination between the two hypotheses. At the present level of exposure, there is no field evidence either for feldspar-rich protoliths from the deeper crust, or for the occurrence of mafic rocks, and the nature of the underlying lower crust is also unknown.

### *9.2.2. Muscovite–biotite leucogranite*

Both the elemental and isotopic compositions of the muscovite–biotite leucogranite (A/CNK values > 1.1; high $SiO_2$ contents, low CaO, MgO, Ba, Sr, $^{87}Sr/^{86}Sr_i > 0.710$, $Nd_i = -7.7$ to $-8.7$, $\delta^{18}O$-wr = 11.33‰, $\delta^{18}O$-zr = 9.5 ± 0.2‰) support a major involvement of metasedimentary sources in the genesis of this magma. Trace element primordial mantle-normalized patterns for the samples from this granite broadly overlap with those of low-grade metapelites and metagreywackes of the SGC, but are comparatively depleted in Sr, HREE and HFSE and enriched in Rb, LREE and P (Fig. 11). The observed HREE and HFSE depletions are consistent with the presence of biotite and minor amounts of garnet in the residual mineral assemblage (Table 4), which would retain the HFSE and the HREE, respectively. The more elevated Rb, LREE and P contents suggest that feldspar + muscovite ± biotite + apatite + monazite were consumed during partial melting reactions. The relatively flat HREE patterns of this granite ($Gd_N/Yb_N$ = 3.4 to 8.6; Fig. 10) indicate a minor role for garnet in the source and, therefore, partial melting at mid crustal levels. This feature is common to many strongly peraluminous granites from the Iberian Variscan belt (e.g. Azevedo et al., 2005; Villaseca et al., 1998, 2008).

Given the high mobility of Rb and Sr during post-magmatic processes, the Sr isotope ratios can be ambiguous. Correlations with potential protoliths must therefore rely mainly on the Nd isotope compositions. The basement in the Aguiar da Beira region is largely composed of Neoproterozoic–Early Cambrian metasediments of the SGC, which includes pelitic sediments (mica-rich, feldspar-poor) and metagreywackes (more enriched in feldspar and quartz). The εNd values for SGC materials, calculated for an age of 320 Ma, range between −8.6 and −11.1 (Teixeira, 2008; Teixeira et al., 2012), providing suitable source lithologies for the leucogranite suite (Fig. 12). The participation of this metasedimentary crust in the genesis of the muscovite–biotite leucogranite can account for both the Nd compositions ($\varepsilon Nd_{317}$ = −7.7 to −8.7) and the relatively high oxygen isotopic compositions ($\delta^{18}O$-wr = 11.33‰, $\delta^{18}O$-zr = 9.5 ± 0.2‰).

Fractional crystallization of a mineral association composed by K-feldspar + plagioclase + quartz + biotite + apatite + monazite + zircon + ilmenite is likely to have played an important role in the evolution of this magma, as suggested by the differentiation trends in variation diagrams, REE patterns and mass balance calculations (discussed below).

## 10. Petrogenetic modeling of the syntectonic muscovite–biotite leucogranite

Simple mass balance calculations for major elements were used to test if the least evolved sample of the muscovite–biotite leucogranite (GN-5) could have been produced by partial melting of a metagreywacke (R14) from the SGC (Teixeira, 2008) composed of quartz, plagioclase, K-feldspar, biotite, muscovite, sillimanite and ilmenite. Attempts to use metapelites from the same metasedimentary sequence as potential protoliths have failed because the composition of the samples did not fit the model and are not presented here.

The model was calculated by adjusting the relative proportions of minerals entering the melt to the composition of the expected magma (GN-5). The quality of the model was assessed through the sum of the squares of the differences between the compositions of the calculated melt and the expected liquid for each element ($\Sigma R^2$). For $\Sigma R^2$ values less than 1.2, the model was considered acceptable (Wyers and Barton, 1986). The results obtained (Table 4) show that it is possible to replicate

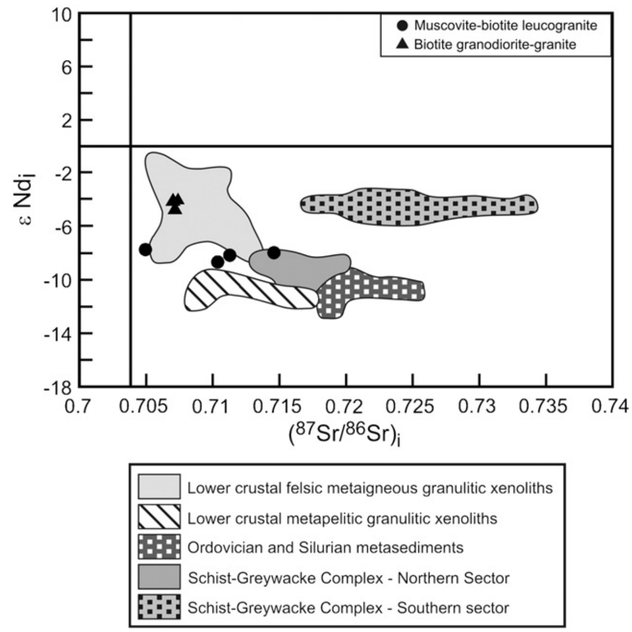


**Fig. 12.** $^{87}Sr/^{86}Sr$ and εNd initial isotopic compositions of samples from the Aguiar da Beira syntectonic granitoids. The plotted fields are recalculated to 320 Ma and were taken from: southern sector of Schist–Greywacke Complex and Ordovician and Silurian metasediments (Beetsma, 1995), northern sector of Schist–Greywacke Complex (Teixeira, 2008), lower crustal pelitic and metaigneous granulitic xenoliths (Villaseca et al., 1999).

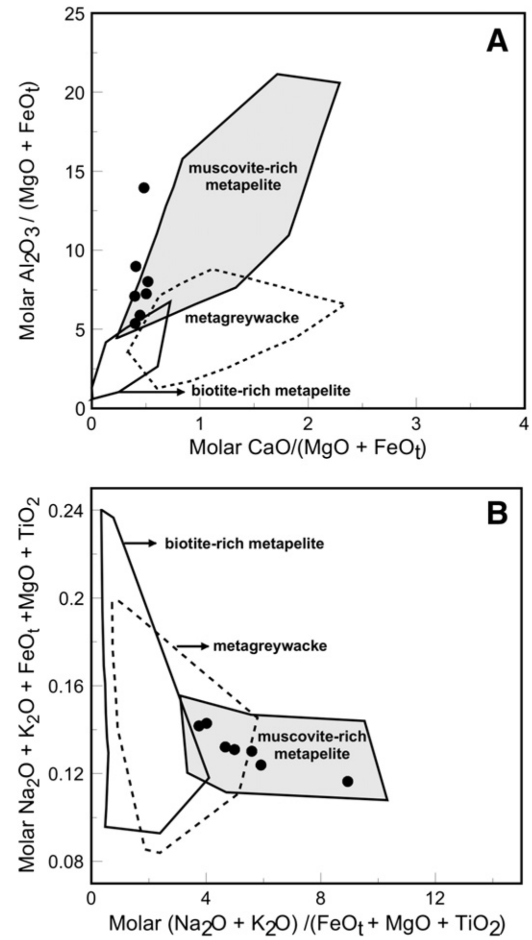


**Fig. 13.** Chemical composition of the Aguiar da Beira muscovite–biotite leucogranite compared with partial melts obtained in experimental studies of mica dehydration melting of metapelites and metagreywackes. Sources: muscovite-rich metapelite field — Patiño Douce and Harris (1998) and Patiño Douce and McCarthy (1998); biotite-rich metapelite field — Le Breton and Thompson (1988), Vielzeuf and Holloway (1988), Patiño-Douce and Johnston (1991), Gardien et al. (1995), Patiño-Douce (1996), and Pickering and Johnston (1998); metagreywacke field — Conrad et al. (1988), Patiño-Douce (1996), Patiño Douce and Beard (1996), Skjerlie and Johnston (1992), Patiño Douce and McCarthy (1998), and Castro et al. (1999). Symbols as in Fig. 4.

the major element composition of sample GN-5 by the anatexis of SGC metagreywacke, leaving a residuum composed by biotite (42%), quartz (21%), sillimanite (20%), plagioclase (7%), cordierite (6%), garnet (3%) and K-feldspar (1%), for a degree of melting (F) of 36% ($\Sigma R^2 = 0.23$).

Melting reactions are likely to be similar to the following (Vielzeuf and Montel, 1994; Vielzeuf and Schmidt, 2001): Ms + Ab + Qtz → Bt + Als + Kfs + melt, and Bt + Als + Pl + Qtz → Grt +Kfs + Melt, where mineral abbreviations are as recommended by Kretz (1983).

Comparison with the major element compositions of glasses obtained from partial melting experiments (e.g. Castro et al., 1999; Montel and Vielzeuf, 1997; Patiño-Douce and Johnston, 1991; Thompson, 1982) reveals, however, that the least evolved samples of muscovite–biotite leucogranite plot close to the boundary between the fields of the melts produced from metagreywacke and muscovite-rich sources in the $Al_2O_3$ / (MgO + $FeO_t$) vs CaO / (MgO + $FeO_t$) diagram (Fig. 13A) and within the domains defined by the same melt types in the $Na_2O + K_2O + FeO_t + MgO + TiO_2$ vs $(Na_2O + K_2O) / FeO_t + MgO + TiO_2$ plot (Fig. 13B). This suggests that both sources could have been involved in the generation of the muscovite–biotite

**Table 4**
Muscovite–biotite leucogranite partial melting major element modeling results.

| | Whole rock wt.% | Protolith composition — metagreywacke (RI4 — Teixeira, 2008) Minerals | | | | | | | | | Produced melt Sample GN5 | Produced melt Calculated composition | Residue Calculated |
|---|---|---|---|---|---|---|---|---|---|---|---|---|---|
| | | Bt | Ilm | Sil | Pl | Grt | Qtz | Fk | Ap | Crd | | | |
| $SiO_2$ | 60.27 | 34.31 | 0.00 | 36.39 | 63.89 | 36.64 | 100.00 | 64.84 | 0.00 | 48.29 | 72.72 | 72.81 | 51.32 |
| $TiO_2$ | 0.91 | 3.16 | 53.00 | 0.04 | 0.00 | 0.01 | 0.00 | 0.00 | 0.00 | 0.00 | 0.18 | 0.10 | 1.34 |
| $Al_2O_3$ | 22.06 | 18.78 | 0.00 | 63.38 | 22.95 | 21.12 | 0.00 | 18.34 | 0.00 | 31.99 | 15.26 | 15.35 | 25.20 |
| $FeO_t$ | 7.03 | 19.31 | 42.00 | 0.00 | 0.10 | 35.07 | 0.00 | 0.01 | 0.00 | 10.70 | 1.26 | 1.42 | 10.00 |
| MnO | 0.05 | 0.24 | 4.74 | 0.00 | 0.00 | 4.90 | 0.00 | 0.00 | 0.00 | 0.27 | 0.02 | −0.37 | 0.29 |
| MgO | 2.66 | 8.05 | 0.00 | 0.00 | 0.00 | 1.78 | 0.00 | 0.02 | 0.00 | 6.69 | 0.41 | 0.40 | 3.86 |
| CaO | 0.46 | 0.04 | 0.00 | 0.00 | 4.01 | 0.76 | 0.00 | 0.00 | 57.00 | 0.04 | 0.63 | 0.70 | 0.31 |
| $Na_2O$ | 1.71 | 0.24 | 0.00 | 0.00 | 9.85 | 0.02 | 0.00 | 2.06 | 0.00 | 0.22 | 3.15 | 3.24 | 0.78 |
| $K_2O$ | 4.72 | 8.91 | 0.00 | 0.00 | 0.07 | 0.00 | 0.00 | 13.93 | 0.00 | 0.00 | 5.88 | 5.97 | 3.87 |
| $P_2O_5$ | 0.14 | 0.00 | 0.00 | 0.00 | 0.00 | 0.00 | 0.00 | 0.31 | 43.00 | 0.00 | 0.49 | 0.38 | 0.00 |
| Total | 100.00 | 93.04 | 99.74 | 99.81 | 100.87 | 100.30 | 100.00 | 99.51 | 100.00 | 98.20 | 100.00 | 100.00 | 96.98 |
| % melt | 0.36 | | | Residue mineralogical composition | | | | | | | | | |
| $\Sigma R^2$ | 0.231 | | | 0.42Bt + 0.21Qtz + 0.20Sil + 0.07Pl + 0.06Cd + 0.03Grt + 0.01Fk | | | | | | | | | |

Bt — biotite; Qtz — quartz; Sil — sillimanite; Pl — plagioclase; Cd — cordierite; Grt — garnet; Fk — K-feldspar; Ap — apatite; Ilm — ilmenite.

**Table 5**
Muscovite–biotite leucogranite fractional crystallization modeling results.

| | Parental magma composition — sample GN-3 | | | | | | | Residual melt | | Cumulate |
|---|---|---|---|---|---|---|---|---|---|---|
| | Whole rock wt.% | Minerals | | | | | | GN-6 | Calculated composition | Calculated composition |
| | | Bt | Pl | Fk | Qtz | Ilm | Ap | | | |
| $SiO_2$ | 72.82 | 35.15 | 67.13 | 64.72 | 100.00 | 0.04 | 0.00 | 74.89 | 74.89 | 67.86 |
| $TiO_2$ | 0.26 | 2.60 | 0.00 | 0.00 | 0.00 | 56.37 | 0.00 | 0.08 | 0.10 | 0.59 |
| $Al_2O_3$ | 15.19 | 18.72 | 19.87 | 18.25 | 0.00 | 0.00 | 0.00 | 15.47 | 15.48 | 14.45 |
| FeO | 1.26 | 22.79 | 0.04 | 0.00 | 0.00 | 40.06 | 0.50 | 0.45 | 0.44 | 2.90 |
| MnO | 0.02 | 0.50 | 0.00 | 0.00 | 0.00 | 4.21 | 1.44 | 0.02 | −0.02 | 0.10 |
| MgO | 0.31 | 4.55 | 0.00 | 0.00 | 0.00 | 0.00 | 0.01 | 0.14 | 0.20 | 0.53 |
| CaO | 0.63 | 0.00 | 0.77 | 0.00 | 0.00 | 0.02 | 53.04 | 0.29 | 0.44 | 1.01 |
| $Na_2O$ | 3.31 | 0.09 | 11.94 | 0.96 | 0.00 | 0.00 | 0.03 | 3.39 | 3.39 | 3.11 |
| $K_2O$ | 5.78 | 9.23 | 0.17 | 15.18 | 0.00 | 0.00 | 0.00 | 4.83 | 4.84 | 7.59 |
| $P_2O_5$ | 0.41 | 0.00 | 0.06 | 0.11 | 0.00 | 0.00 | 41.78 | 0.43 | 0.25 | 0.72 |
| Total | 100.00 | 93.63 | 99.98 | 99.22 | 100.00 | 100.70 | 96.80 | 100.00 | 100.00 | 98.87 |
| % crystallization | 34% | | | Cumulate mineral composition | | | | | | |
| $\Sigma R^2$ | 0.055 | | | 0.43Fk + 0.23Pl + 0.21Qtz + 0.12Bt + 0.02Ap + 0.01Ilm | | | | | | |

Trace element modeling

Rayleigh's equation — $CL / CL_0 = F^{D-1}$

| | $CL_0$ | | F = 0.66 | KDs used | | | |
|---|---|---|---|---|---|---|---|
| | GN3 | GN6 | CL | Biotite | K-feldspar | Plagioclase | |
| Sr | 56 | 31 | 28 | 7.20 | 2.00 | 4.04 | Arth (1976), Mahood and Hildreth (1983), Stix and Gorton (1990), Jolliff et al. (1992), Bea et al. (1994), and Ewart and Griffin (1994). |
| Ba | 191 | 81 | 81 | 3.70 | 6.00 | 0.19 | |
| Rb | 475 | 538 | 517 | 4.00 | 0.70 | 0.06 | |

CL _ trace element composition in the residual melt; $C_O$ — trace element composition in the parental magma; F — residual melt fraction; D — global partition coefficient. Sr, Ba and Rb contents in ppm. Bt — biotite; Qtz — quartz; Pl — plagioclase; Fk — K-feldspar; Ap — apatite; Ilm — ilmenite.

leucogranite. In fact, the dehydration of metapelites, that are also part of the SGC, and mica-enriched, must have played an important role in providing some of the water required to melt the metagreywackes.

The suggested and modeled derivation from mid-crustal metasedimentary protoliths for the muscovite–biotite leucogranite from Aguiar da Beira is in agreement with other studies of similar syntectonic intrusions (e.g. Azevedo et al., 2005; Beetsma, 1995; Neiva and Gomes, 2001; Teixeira, 2008; Valle Aguado et al., 2005; Villaseca et al., 2008). Furthermore, it evidences that the petrogenetic processes and/or the protoliths involved in magma genesis changed from the production of syntectonic to the post-tectonic Iberian Variscan leucogranitic magmas, as for the later leucogranites, given their less radiogenic (Sr–Nd–O) signatures, other origins have been proposed, such as a derivation from metaigneous lower crustal sources (Villaseca et al., 2012) or the addition of mantle magmas to crust-derived melts (e.g. Castro et al., 1999; Dias et al., 2002; Silva et al., 2000).

The fractional crystallization hypothesis has also been tested using the general least-squares mixing equation devised by Le Maitre (1981). Examples of the output are given in Table 5. In the calculation of this model, one of the most primitive samples was chosen to represent the composition of the presumed parental magma and the sample with the highest $SiO_2$ content (GN-6) to simulate the fractionated melt. Major-element based least-squares modeling reveals that the geochemical variation observed within the muscovite–biotite leucogranite can be accounted for by up to 34% fractionation of a mineral assemblage consisting of K-feldspar (43%), plagioclase (23%), quartz (21%), biotite (12%), apatite (2%) and ilmenite (1%). Statistical fit is excellent ($\Sigma R^2 = 0.06$).

On the basis of the major element model results and partition coefficients from the literature (Table 5), further calculations were performed using the Rayleigh's fractionation equation (Arth, 1976) to predict the behavior of some trace elements (Ba, Rb, Sr) during fractional crystallization. Cumulate compositions and *F* values estimated from major element modeling were used to derive the Ba–Rb–Sr models and the results demonstrate that crystal fractionation has probably played a significant role in the evolution of the Aguiar da Beira peraluminous leucogranite suite.

## 11. Concluding remarks

Given the apparent synchronous emplacement of both Aguiar da Beira syntectonic granitoids (322–317 Ma) and the intracontinental shearing that characterized the $D_3$ Variscan deformation event, it may be presumed that the steep $D_3$ shear zones could have acted as structural conduits for the ascent of these magmas and that their emplacement occurred in an essentially transcurrent regime related to strike-slip, sinistral and dextral subvertical shear zones ($D_3$). While the overall chemical and isotopic signature of the muscovite–biotite leucogranite can well be explained by partial melting of an old supracrustal metasedimentary source, with high $^{87}Sr/^{86}Sr_t$ and low $\varepsilon Nd_t$, the genesis of the biotite granodiorite–granite suite appears to require a less radiogenic metaigneous crustal source or mixing of lower crustal and mantle derived magmas. Decompression melting of mid-upper crust metasedimentary rocks, triggered by the $D_2$ extensional event related to crustal gravitational collapse, could account for the origin of the leucogranite suite, whereas mantle melting and concomitant underplating of the lower crust is one of the possible mechanisms to explain the generation of the biotite granodiorite–granite suite.

## Acknowledgments

The first author benefited from the support from a PhD grant (SFRH/BD/2005/21410) and from a grant awarded in the scope of the PETROCHRON research project (PTDC/CTE-GIX/112561/2009), both sponsored by FCT (Science and Technology Foundation, Ministry of Education and Science, Portugal). Prof. Andrés Cuesta Fernandez is kindly acknowledged for the facilities at the Laboratório de Geologia e Geocronologia of the University of Oviedo, Spain and Eng. Sara Ribeiro for the technical assistance with the whole-rock Rb–Sr and Sm–Nd isotopic analyses at the Laboratory of Isotope Geology of the University of Aveiro, Portugal. Martin Whitehouse, Lev Ilyinsky, and Yaron

Be'eri-Shlevin at Nordsim are thanked for the assistance in measuring the oxygen composition of zircon. The Nordsim facility is a joint Nordic infrastructure supported by the research funding agencies of Denmark, Iceland, Norway and Finland and the Geological Survey of Finland; this is Nordsim contribution #366. The authors also thank Dr. Marlina Elburg, an anonymous reviewer and Dr. Nelson Eby for their constructive comments.

## Appendix 1. Zircon oxygen isotope individual analysis of each of the samples analyzed from the biotite granodiorite–granite and the muscovite–biotite leucogranite

| Spot ID | Background corrected | | $\delta^{18}O^{a}_{V\text{-}SMOW}$ | |
|---|---|---|---|---|
| | $^{18}O/^{16}O$ | $\pm 1\sigma$ (abs) | ‰ | $\pm 1\sigma$ (abs) |
| *Biotite granodiorite–granite — sample SER-3* | | | | |
| 01 a — lp tip | 0.00201877 | 0.00000041 | 8.57 | 0.31 |
| 01b — lp other tip | 0.00201743 | 0.00000047 | 7.90 | 0.33 |
| 02a — lp tip | 0.00201830 | 0.00000048 | 8.34 | 0.34 |
| 02b[a] — lp edge of tip | 0.00201457 | 0.00000041 | 6.47 | 0.31 |
| 02c — lp center | 0.00201774 | 0.00000026 | 8.07 | 0.29 |
| 03a — lp tip | 0.00201852 | 0.00000027 | 8.46 | 0.29 |
| 03b — lp center | 0.00201757 | 0.00000030 | 7.99 | 0.30 |
| 03c — lp tip | 0.00201805 | 0.00000028 | 8.23 | 0.29 |
| 04a — lp tip | 0.00201716 | 0.00000043 | 7.78 | 0.33 |
| 04b — lp tip | 0.00201652 | 0.00000031 | 7.46 | 0.30 |
| 05a[a] — lp edge of tip | 0.00201519 | 0.00000026 | 6.80 | 0.29 |
| 06a — lp tip | 0.00201752 | 0.00000038 | 7.96 | 0.32 |
| 06b — lp center, alt | 0.00201739 | 0.00000044 | 7.90 | 0.34 |
| 07a — lp tip | 0.00201740 | 0.00000059 | 7.90 | 0.39 |
| Average of 12 spots (without 2b, 5a) | | | 8.05 | $\pm 0.31$ ($2\sigma$m) |
| *Muscovite–biotite leucogranite — sample GN3* | | | | |
| 01 — isolated tip | 0.00202040 | 0.00000043 | 9.39 | 0.32 |
| 03 — lp tip | 0.00202046 | 0.00000046 | 9.42 | 0.33 |
| 04 — lp tip | 0.00202037 | 0.00000055 | 9.37 | 0.36 |
| 05a — lp tip | 0.00202109 | 0.00000027 | 9.75 | 0.29 |
| 07a — lp center | 0.00202065 | 0.00000040 | 9.53 | 0.33 |
| 07b — lp tip, alt | 0.00202083 | 0.00000042 | 9.61 | 0.33 |
| 08a — lp tip | 0.00202091 | 0.00000038 | 9.65 | 0.32 |
| 09a — lp tip | 0.00201991 | 0.00000023 | 9.15 | 0.28 |
| Average of 8 spots | | | 9.48 | $\pm 0.19$ ($2\sigma$m) |

[a]Normalized to a $\delta^{18}O$ value of 9.86‰ for the 91500 standard. The instrumental mass fractionation correction and the reported uncertainty are based on 83 standards measurements with an external precision of 0.26‰ that has been propagated onto the internal uncertainty to yield an overall value. Abbreviations: lp = long prism (length to width = 4–7), alt = altered domain.

## Appendix 2. Supplementary data

Supplementary data to this article can be found online at http://dx.doi.org/10.1016/j.lithos.2014.02.023.

## References


Arenas, R., Catalán, J.R.M., 2003. Low-P metamorphism following a Barrovian-type evolution. Complex tectonic controls for a common transition, as deduced in the Mondoñedo thrust sheet (NW Iberian Massif). Tectonophysics 365, 143–164.

Arth, J.G., 1976. Behavior of trace elements during magmatic processes — a summary of theoretical models and their applications. Journal of Research of the U.S. Geological Survey 4, 41–47.

Azevedo, M., Valle Aguado, B., Nolan, J., Martins, M., Medina, J., 2005. Origin and emplacement of syn-orogenic Variscan granitoids in Iberia the Beiras massif. In: Carosi, R., Dias, R., Iacopini, D., Rosenbaum, G. (Eds.), The Southern Variscan Belt, Journal of the Virtual Explorer, Electronic Edition, 19 (Paper 7).

Barbarin, B., 2005. Mafic magmatic enclaves and mafic rocks associated with some granitoids of the central Sierra Nevada batholith, California: nature, origin, and relations with the hosts. Lithos 80, 155–177.

Barbarin, B., Didier, J., 1992. Genesis and evolution of mafic microgranular enclaves through various types of interaction between coexisting felsic and mafic magmas. Transactions of Royal Society of Edinburg Earth Science 83, 145–153.

Bea, F., Pereira, M.D., Stroh, A., 1994. Mineral/leucosome trace-element partitioning in a peraluminous migmatite (a laser ablation-ICP-MS study). Chemical Geology 117, 291–312.

Beetsma, J.J., 1995. The Late Proterozoic/Paleozoic and Hercynian Crustal Evolution of the Iberian Massif, N Portugal. (Ph.D. Thesis) Vrije University, Netherlands 223.

Bosse, V., Boulvais, P., Gautier, P., Tiepolo, M., Ruffet, G., Devidal, J.L., Cherneva, Z., Gerdjikov, I., Paquette, J.L., 2009. Fluid-induced disturbance of the monazite Th–Pb chronometer: in situ dating and element mapping in pegmatites from the Rhodope (Greece, Bulgaria). Chemical Geology 261, 286–302.

Castro, A., Patiño Douce, A.E., Corretgé, L.G., De la Rosa, J.D., El-Biad, M., El-Himidi, H., 1999. Origin of peraluminous granites and granodiorites, Iberian massif, Spain: an experimental test of granite petrogenesis. Contributions to Mineralogy and Petrology 135, 255–276.

Castro, A., Corretge, L.G., De la Rosa, J., Fernandez, C., Lopez, S., Garcia-Moreno, O., Chacon, H., 2003. The appinite–migmatite complex of Sanabria, NW Iberian massif, Spain. Journal of Petrology 44, 1309–1344.

Cherniak, D.J., Watson, E.B., 2000. Pb diffusion in zircon. Chemical Geology 172, 5–24.

Cherniak, D.J., Watson, E.B., Grove, M., Harrison, T.M., 2004. Pb diffusion in monazite: a combined RBS/SIMS study. Geochimica et Cosmochimica Acta 68 (4), 829–840.

Clayton, R.N., Mayeda, T., 1963. The use of bromine pentafluoride in the extraction of oxygen from oxides and silicates for isotopic analysis. Geochimica et Cosmochimica Acta 27, 47–52.

Conrad, W.K., Nicholls, I.A., Wall, V.J., 1988. Water-saturated and undersaturated melting at 10 kbar: evidence for the origin of silicic magmas in the Taupo Volcanic Zone, New Zealand, and other occurrences. Journal of Petrology 29, 765–803.

Corfu, F., 2004. U–Pb age, setting and tectonic significance of the anorthosite–mangerite–charnockite–granite suite, Lofoten-Vesterålen, Norway. Journal of Petrology 56, 2081–2097.

Corfu, F., Hanchar, J.M., Hoskin, P.W.O., Kinny, P., 2003. Atlas of zircon textures. In: Hanchar, J.M., Hoskin, P.W.O. (Eds.), Zircon: Mineralogical Society of America, 53, pp. 468–500.

Dallmeyer, R.D., Martínez Catalán, J.R., Arenas, R., Gil Ibarguchi, J.I., Gutiérrez Alonso, G., Farias, P., Bastida, F., Aller, J., 1997. Diachronous Variscan tectonothermal activity in the NW Iberian Massif: evidence from $^{40}Ar/^{39}Ar$ dating of regional fabrics. Tectonophysics 277, 307–337.

Davies, D.W., Blackburn, C.E., Krogh, T.E., 1982. Zircon U–Pb ages from the Wabigoon, Manitou Lakes Region, Wabigoon Subprovince, northwest Ontario. Canadian Journal of Earth Sciences 19, 254–266.

Debon, F., Lefort, P., 1988. A cationic classification of common plutonic rocks and their magmatic associations — principles, method, applications. Bulletin de Mineralogie 111, 493–510.

DePaolo, D.J., 1981. Neodymium isotopes in the Colorado Front Range and crust mantle evolution in the Proterozoic. Nature 291, 193–196.

DePaolo, D.J., 1988. Neodymium Isotope Geochemistry: An Introduction. Springer Verlag, New York (187 pp.).

Dias, R., Ribeiro, A., 1995. The Ibero-Armorican Arc: a collision effect against an irregular continent? Tectonophysics 246, 113–128.

Dias, G., Leterrier, J., Mendes, A., Simoes, P.P., Bertrand, J.M., 1998. U–Pb zircon and monazite geochronology of post-collisional Hercynian granitoids from the Central Iberian Zone (Northern Portugal). Lithos 45, 349–369.

Dias, G., Simões, P.P., Ferreira, N., Leterrier, J., 2002. Mantle and crustal sources in the genesis of late-Hercynian granitoids (NW Portugal): geochemical and Sr–Nd isotopic constraints. Gondwana Research 5 (2), 287–305.

Escuder Viruete, J., Arenas, R., Martínez Catalán, J.R., 1994. Tectonothermal evolution associated with Variscan crustal extension in the Tormes Gneiss Dome (NW Salamanca, Iberian Massif, Spain). Tectonophysics 238, 117–138.

Ewart, A., Griffin, W.L., 1994. Application of proton-microprobe data to trace-element partitioning in volcanic-rocks. Chemical Geology 117 (1–4), 251–284.

Fernández-Suárez, J., Dunning, G.R., Jenner, G.A., Gutíerrez-Alonso, G., 2000. Variscan collisional magmatism and deformation in NW Iberia: constraints from U–Pb geochronology of granitoids. Journal of the Geological Society 157, 565–576.

Fernández-Suárez, J., Gutierrez-Alonso, G., Jeffries, T.E., 2002. The importance of along-margin terrane transport in northern Gondwana: insights from detrital zircon parentage in Neoproterozoic rocks from Iberia and Brittany. Earth and Planetary Science Letters 204 (1–2), 75–88.

Fernández-Suárez, J., Gutiérrez-Alonso, G., Johnston, S.T., Jeffries, T.E., Pastor-Galan, D., Jenner, G.A., Murphy, J.B., 2011. Iberian late-Variscan granitoids: some considerations on crustal sources and the significance of "mantle extraction ages". Lithos 123, 121–132.

Frost, B.R., Arculus, R.J., Barnes, C.G., Collins, W.J., Ellis, D.J., Frost, C.D., 2001. A geochemical classification of granitic rocks. Journal of Petrology 42, 2033–2048.

Gardien, V., Thompson, A.B., Grujic, G., Ulmer, P., 1995. Experimental melting of biotite + plagioclase + quartz ± muscovite assemblages and implications for crustal melting. Journal of Geophysical Research 100 (B8), 15581–15591.

Goldstein, S.J., Jacobsen, S.B., 1988. Nd and Sr isotopic systematics of river water suspended material — implications for crustal evolution. Earth and Planetary Science Letters 87 (3), 249–265.

Gutiérrez-Alonso, G., Fernández-Suárez, J., Jeffries, T.E., Johnston, S.T., Pastor-Galán, D., Murphy, J.B., Franco, M.P., Gonzalo, J.C., 2011. Diachronous post-orogenic magmatism within a developing orocline in Iberia, European Variscides. Tectonics 30 (TC5008), 17.

Haskin, L.A., Haskin, M.A., Frey, F.A., Wildman, T.R., 1968. Relative and absolute terrestrial abundances of the rare earths. In: Ahrens, L.H. (Ed.), Origin and Distribution of the Elements, 1. Pergamon, Oxford, pp. 889–911.

Hawkins, D.P., Bowring, S.A., 1997. U–Pb systematics of monazite and xenotime: case studies from the Paleoproterozoic of the Grand Canyon, Arizona. Contributions to Mineralogy and Petrology 127, 87–103.

Hoefs, 2004. Stable Isotopic Geochemistry, 5th ed. Springer Verlag, Germany.

Jacobsen, S.B., Wasserburg, G.J., 1980. Sm–Nd isotopic evolution of chondrites. Earth and Planetary Science Letters 50, 139–155.

Jaffey, A.H., Flynn, K.F., Glendenin, L.E., Bentley, W.C., Essling, A.M., 1971. Precision measurement of half-lives and specific activities of $^{235}U$ and $^{238}U$. Physical Review Section C, Nuclear Physics 4, 1889–1906.

Jolliff, B.L., Papike, J.J., Shearer, C.K., 1992. Petrogenetic relationships between pegmatite and granite based on geochemistry of muscovite in pegmatite wall zones, Black Hills, South Dakota, U.S.A. Geochimica et Cosmochimica Acta 56, 1915–1939.

Karioris, F.G., Gowda, K.A., Carrz, L., 1981. Heavy ion bombardment on monoclinic $ThSiO_4$, $ThO_2$, and monazite. Radiation Effects Letters 58, 1–3.

Kretz, R., 1983. Symbols for rock-forming minerals. American Mineralogist 68, 277–279.

Krogh, T.E., 1973. A low contamination method for hydrothermal decomposition of zircon and extraction of U and Pb for isotopic age determinations. Geochimica et Cosmochimica Acta 37, 485–494.

Krogh, T.E., 1982. Improved accuracy of U–Pb zircon ages by creation of more concordant systems using an air abrasion technique. Geochimica et Cosmochimica Acta 46, 637–649.

La Roche, H., Leterrier, J., GrandClaude, P., Marchal, M., 1980. A classification of volcanic and plutonic rocks using R1–R2 diagram and major element analyses — its relationships with current nomenclature. Chemical Geology 29, 183–210.

Le Breton, N., Thompson, A.B., 1988. Fluid-absent (dehydration) melting of biotite in metapelites in the early stages of crustal anatexis. Contributions to Mineralogy and Petrology 99, 226–237.

Le Maitre, R.W., 1981. GENMIX—a generalised petrological mixing model program. Computers and Geosciences 7, 229–247.

LNEG, 2010. Carta Geológica de Portugal à escala 1:1000000, edição de 2010, Laboratório Nacional de Engenharia e Geologia — Laboratório de Geologia e Minas, Lisboa.

Ludwig, K.R., 2003. Users manual for Isoplot 3.00. Berkeley Geochronology Center Special Publication 4 (70 pp.).

Mahood, G., Hildreth, W., 1983. Large partition coefficients for trace elements in high-silica rhyolites. Geochimica et Cosmochimica Acta 54, 2015–2050.

Martínez Catalán, J.R., Arenas, R., Garcia, F.D., Cuadra, P.G., Gomez-Barreiro, J., Abati, J., Castiñeiras, P., Fernández-Suárez, J., Martinez, S.S., Andonaegui, P., Gonzalez Oavijo, E., Diez Montes, A., Rubio Pascual, F.J., Valle Aguado, B., 2007. Space and time in the tectonic evolution of the northwestern Iberian Massif: implications for the Variscan belt, in 4-D Framework of Continental Crust. In: Hatcher Jr., R.D., Carlson, M.P., McBride, J.H., Martínez Catalán, J.R. (Eds.), 4-D Framework of Continental Crust. Geological Society of America Memoir, 200D, pp. 403–423.

Martínez Catalán, J.R., Arenas, R., Abati, J., Sánchez Martinez, S., Diaz Garcia, E., Fernández-Suarez, J., Gonzalez Cuadra, P., Castineiras, P., Gomez Barreiro, J., Diez Montes, A., Gonzalez Clavijo, E., Rubio Pascual, F.J., Andonaegui, P., Jeffries, T.E., Alcock, J.E., Diez Fernandez, R., Lopez Carmona, A., 2009. A rootless suture and the loss of the roots of a mountain chain: the Variscan Belt of NW Iberia. Comptes Rendus Geoscience 341, 114–126.

McLennan, S.M., Taylor, S.R., 1996. Heat flow and the chemical ultramafic rocks from Val Sesia, the Ivrea Zone, NW Italy: trace composition of continental crust. Journal of Geology 104, 369–377.

Miller, C.F., McDowell, S.M., Mapes, R.W., 2003. Hot and cold granites? Implications of zircon saturation temperatures and preservation of inheritance. Geology 31, 529–532.

Montel, J.M., Vielzeuf, D., 1997. Partial melting of metagreywackes, Part II. Compositions of minerals and melts. Contributions to Mineralogy and Petrology 128, 176–196.

Murphy, J.B., Gutierrez-Alonso, G., Fernandez-Suarez, J., Braid, J.A., 2008. Probing crustal and mantle lithosphere origin through Ordovician volcanic rocks along the Iberian passive margin of Gondwana. Tectonophysics 461, 166–180.

Nachit, H., Razafimahefa, N., Stussi, J.M., Carron, J.P., 1985. Composition chimique des biotites et typologie magmatique des granitoïdes. Comptes Rendus de l'Académie des Sciences de Paris 301 (11), 813–818.

Neiva, A.M.R., Gomes, M.E.P., 2001. Diferentes tipos de granitos e seus processos petrogenéticos: granitos Hercínicos portugueses. Memórias Academia das Ciências de Lisboa XXXIX, 53–95.

Noronha, F., Ramos, J.M.F., Rebelo, J.A., Ribeiro, A., Ribeiro, M.L., 1981. Essai de corrélation des phases de déformation hercyniennes dans le nord-ouest Péninsulaire. Leidse Geologische Mededel 52, 87–91.

Oliveira, J.T., Pereira, E., Piçarra, J.M., Young, T., Romano, M., 1992. O Paleozóico Inferior de Portugal: síntese da estratigrafia e da evolução paleogeográfica. In: Saavedra, J., Rábano, I., Gutiérrez Marco, J.G. (Eds.), Paleozoico Inferior de Ibero-América. Universidade de Extremadura, pp. 359–374.

Patiño Douce, A.E., Beard, J.S., 1996. Effects of P, $f(O_2)$ and Mg/Fe ratio on dehydration-melting of model metagreywackes. Journal of Petrology 37, 999–1024.

Patiño Douce, A.E., Harris, N., 1998. Experimental constraints on Himalayan Anatexis. Journal of Petrology 39, 689–710.

Patiño Douce, A.E., McCarthy, T.C., 1998. Melting of crustal rocks during continental collision and subduction. In: Hacker, B.R., Liou, J.G. (Eds.), When Continents Collide: Geodynamics and Geochemistry of Ultrahigh-Pressure Rocks. Kluwer Academic, Dordrecht, pp. 27–55.

Patiño-Douce, A.E., 1996. Effects of pressure and $H_2O$ content on the compositions of primary crustal melts. Transactions of the Royal Society of Edinburg: Earth Sciences 87, 11–21.

Patiño-Douce, A.E., Johnston, A.D., 1991. Phase equilibria and melt productivity in the pelitic system: implications for the origin of peraluminous granitoids and aluminous granulites. Contributions to Mineralogy and Petrology 107, 202–218.

Pickering, J.M., Johnston, A.D., 1998. Fluid-absent melting behavior of a two-mica metapelite: experimental constraints on the origin of Black Hills granite. Journal of Petrology 39, 1788–1804.

Poitrasson, F., Chenery, S., Bland, D.J., 1996. Contrasted monazite hydrothermal alteration mechanisms and their geochemical implications. Earth and Planetary Science Letters 145, 79–96.

Poitrasson, F., Chenery, S., Shepherd, T.J., 2000. Electron microprobe and LA-ICP-MS study of monazite hydrothermal alteration: implications for U–Th–Pb geochronology and nuclear ceramics. Geochimica et Cosmochimica Acta 64, 3283–3297.

Ribeiro, A., Quesada, C., Dallmeyer, R.D., 1990. Geodynamic evolution of the Iberian Massif. In: Dallmeyer, R.D., Garcia, Martínez (Eds.), Pre-Mesozoic Geology of Iberia, pp. 399–409.

Robardet, M., 2002. Alternative approach to the Variscan Belt in Southwestern Europe: preorogenic paleobiogeographical constraints. In: Martínez-Catalán, J. R., Hatcher, R.D., Arenas, R., Díaz García, F. (Eds.), Variscan–Appalachian Dynamics: The Building of the Late Paleozoic Basement. Geological Society of America Special Paper, pp. 1–15.

Robardet, M., 2003. The Armorica 'microplate': fact or fiction? Critical review of the concept and contradictory palaeobiogeographical data. Palaeogeography, Palaeoclimatology, Palaeoecology 195, 125–148.

Roberts, M.P., Clemens, J.D., 1993. The origin of high-K, calcalkaline, I-type granitoid magmas. Geology 21, 825–882.

Rodríguez Alonso, M.D., Díez Balda, M.A., Perejón, A., Pieren, A., Liñán, E., López Díaz, F., Moreno, F., Gámez Vintaned, J.A., Gónzalez Lodeiro, F., Martínez Poyatos, D., Vegas, R., 2004. Domínio del Complejo Esquisto-Grauváquico: Estratigrafía. In: Vera, J.A. (Ed.), Geología de España. SGE-IGME, Madrid, pp. 78–81.

Sánchez-García, T., Quesada, C., Bellido, F., Dunning, G.R., González del Tánago, J., 2008. Two-step magma flooding of the upper crust during rifting: the Early Paleozoic of the Ossa–Morena Zone (SW Iberia). Tectonophysics 461, 72–90.

Seydoux-Guillaume, A.M., Paquette, J.L., Wiedenbeck, M., Montel, J.M., Heinrich, W., 2002. Experimental resetting of the U–Th–Pb systems in monazite. Chemical Geology 191, 165–181.

Silva, M.M.V.G., Neiva, A.M.R., Whitehouse, M.J., 2000. Geochemistry of enclaves and host granites from Nelas area, central Portugal. Lithos 50, 153–170.

Skjerlie, K.P., Johnston, A.D., 1992. Vapor-absent melting at 10 kbar of biotite- and amphibole-bearing tonalitic gneiss: implication for the generation of A-type granites. Geology 20, 263–266.

Sousa, M.B., 1984. Considerações paleogeográficas sobre a estratigrafia do Complexo Xisto-Grauváquico (CXG) e sua relação com o Paleozóico Inferior. Cuadernos de Geologia Iberica 9, 9–36.

Stacey, J.S., Kramers, J.D., 1975. Approximation of terrestrial lead isotope evolution by a two-stage model. Earth and Planetary Science Letters 34, 207–226.

Stix, J., Gorton, M.P., 1990. Variations in sanidine partition coefficients in the Cerro Toledo Rhyolite, Jemez Mountains, New Mexico: effects of composition, temperature, and volatiles. Geochimica et Cosmochimica Acta 54, 2697–2708.

Sun, S.-S., McDonough, W.F., 1989. Chemical and isotopic systematics of oceanic basalts: implications for mantle composition and processes. In: Saunders, A.D., Norry, M.J. (Eds.), Magmatism in Ocean Basins. Geological Society Special Publication, pp. 313–345.

Teixeira, R.S.T., 2008. Mineralogia, petrologia e geoquímica dos granitos e seus encraves da região de Carrazeda de Ansiães. (PhD Thesis) Universidade de Trás-os-Montes e Alto Douro, Portugal 427.

Teixeira, C., Santos, J.P., Lopes, J.V.T., Pilar, L., Pereira, V.C., 1972. Carta Geológica de Portugal, escala 1: 50000, Folha 14D (Aguiar da Beira) e respectiva notícia explicativa. Serviços Geológicos de Portugal, Lisboa.

Teixeira, R.J.S., Neiva, A.M.R., Gomes, M.E.P., Corfu, F., Cuesta, A., Croudace, I.W., 2012. The role of fractional crystallization in the genesis of early syn-$D_3$, tin-mineralized Variscan two-mica granites from the Carrazeda de Ansiães area, northern Portugal. Lithos 153, 177–191.

Teufel, S., Heinrich, W., 1997. Partial resetting of the U–Pb isotope system in monazite through hydrothermal experiments: an SEM and U–Pb isotope study. Chemical Geology 137, 273–281.

Thompson, A.B., 1982. Dehydration melting of pelitic rocks and the generation of $H_2O$-undersaturated granitic liquids. American Journal of Science 282, 1567–1595.

Townsend, K.J., Miller, C.F., D'Andrea, J.L., Ayers, J.C., Harrison, T.M., Coath, C.D., 2001. Low temperature replacement of monazite in the Ireteba granite, Southern Nevada: geochronological implications. Chemical Geology 172, 95–112.

Valle Aguado, B., Azevedo, M.R., Schaltegger, U., Martinez Catalán, J.R., Nolan, J., 2005. U–Pb zircon and monazite geochronology of Variscan magmatism related to synconvergence extension in Central Northern Portugal. Lithos 82, 169–184.

Vernon, R.H., 1984. Microgranitoid enclaves in granites: globules of hybrid magma quenched in a plutonic environment. Nature 309, 438–439.

Vernon, R.H., 1990. Crystallization and hybridism in microgranitoid enclave magmas: microstructural evidence. Journal of Geophysical Research 95, 17849–17859.

Vernon, R.H., 1991. Interpretation of microstructures of microgranitoid enclaves. In: Didier, J., Barbarin, B. (Eds.), Enclaves and Granite Petrology. Developments in Petrology, 13, pp. 277–292.

Vielzeuf, D., Holloway, J.R., 1988. Experimental determination of the fluid-absent melting relations in the pelitic system: consequences for crustal differentiation. Contributions to Mineralogy and Petrology 98, 257–276.

Vielzeuf, D., Montel, J.M., 1994. Partial melting of metagreywackes. Part 1. Fluid-absent experiments and phase relationships. Contributions to Mineralogy and Petrology 117, 375–393.

Vielzeuf, D., Schmidt, M.W., 2001. Melting relations in hydrous systems revisited: applications to pelites, greywackes and basalts. Contributions to Mineralogy and Petrology 141, 251–267.

Villaseca, C., Barbero, L., Rogers, G., 1998. Crustal origin of Hercynian peraluminous granitic batholiths of central Spain: petrological, geochemical and isotopic (Sr, Nd) constraints. Lithos 43, 55–79.

Villaseca, C., Downes, H., Pin, C., Barbero, L., 1999. Nature and composition of the lower continental crust in central Spain and the granulite–granite linkage: inferences from granulitic xenoliths. Journal of Petrology 40, 1465–1496.

Villaseca, C., Pérez-Soba, C., Merino, E., Orejana, D., López-García, J.A., Billstrom, K., 2008. Contrasting crustal sources for peraluminous granites of the segmented Montes de Toledo Batholith (IberianVariscan Belt). Journal of Geosciences 53, 263–280.

Villaseca, C., Bellido, F., Pérez-Soba, C., Billström, K., 2009. Multiple crustal sources for post-tectonic I-type granites in the Hercynian Iberian Belt. Mineralogy and Petrology 96, 197–211.

Villaseca, C., Orejana, D., Belousova, E., Armstrong, A., Pérez-Soba, C., Jeffries, T., 2012. U–Pb isotopic ages and Hf isotope composition of zircons in Variscan gabbros from central Spain: evidence of variable crustal contamination. Mineralogy and Petrology 101 (3), 151–167.

Watson, E.B., Harrison, T.M., 1983. Zircon saturation revisited: temperature and composition effects in a variety of crustal magma types. Earth and Planetary Science Letters 64, 295–304.

Wedepohl, K.H., 1995. The composition of the continental crust. Geochimica et Cosmochimica Acta 59, 1217–1232.

Whitehouse, M.J., Nemchin, A.A., 2009. High precision, high accuracy measurement of oxygen isotopes in a large lunar zircon by SIMS. Chemical Geology 261, 32–42.

Wiedenbeck, M., Hanchar, J., Peck, W.H., Sylvester, P., Valley, J., Whitehouse, M., Kronz, A., Morishita, Y., Nasdala, L., 2004. Further characterization of the 91500 zircon crystal. Geostandards and Geoanalytical Research 28, 9–39.

Wilson, M., 1989. Igneous petrogenesis. A Global Tectonic ApproachUnwin Hyman, London (466 pp.).

Wyers, G.P., Barton, M., 1986. Petrology and evolution of transitional alkaline-subalkaline lavas from Patmos, Dodecanesos, Greece: evidence for fractional crystallization, magma mixing, and assimilation. Contributions to Mineralogy and Petrology 93, 297–311.